

CHARACTERIZING BARS AT $Z \sim 0$ IN THE OPTICAL AND NIR: IMPLICATIONS FOR THE EVOLUTION OF BARRED DISKS WITH REDSHIFT

IRINA MARINOVA¹, SHARDHA JOGEE¹
 marinova@astro.as.utexas.edu, sj@astro.as.utexas.edu
 Draft version October 21, 2018

ABSTRACT

Critical insights on galaxy evolution stem from the study of bars. With the advent of high redshift *HST* surveys that trace bars in the rest-frame optical band out to $z \sim 1$, it becomes increasingly important to provide a reference baseline for bars at $z \sim 0$ in the optical band. We present results on bars at $z \sim 0$ in the optical and near-infrared bands, based on 180 spirals in the OSUBSGS survey. (1) The deprojected bar fraction at $z \sim 0$ is $f_{\text{NIR1}} \sim 60\% \pm 6\%$ in the near-infrared *H* band, and $f_{\text{optical1}} \sim 44\% \pm 6\%$ in the optical *B*-band images. The latter likely miss bars obscured by dust and star formation. (2) The results before and after deprojection are similar, which is encouraging for high redshift studies that forego deprojection. (3) Studies of bars at $z \sim 0.2$ – 1.0 (lookback times of 3–8 Gyr) have reported an optical bar fraction of $f_{\text{optical2}} \sim 30\% \pm 6\%$, after applying cutoffs in absolute magnitude ($M_V < -19.3$), bar size ($a_{\text{bar}} \geq 1.5$ kpc), and bar ellipticity ($e_{\text{bar}} \geq 0.4$) in order to ensure a complete sample, adequate spatial resolution, and reliable bar identification out to $z \sim 1$. Applying these exact cutoffs in magnitude, bar size, and bar ellipticity to the OSUBSGS data yields a comparable optical *B*-band bar fraction at $z \sim 0$ of $f_{\text{optical3}} \sim 34\% \pm 6\%$. This rules out scenarios where the optical bar fraction in bright disks declines strongly with redshift. (4) We investigate bar strengths at $z \sim 0$ using the maximum bar ellipticity (e_{bar}) as a guide. Most ($\sim 70\%$) bars have moderate to high ellipticity ($0.50 \leq e_{\text{bar}} \leq 0.75$), and only a small fraction (7%–10%) have $0.25 \leq e_{\text{bar}} \leq 0.40$. There is no bimodality in the distribution of e_{bar} . The *H*-band bar fraction and e_{bar} show no substantial variation across RC3 Hubble types Sa to Scd. (5) RC3 bar types should be used with caution. Many galaxies with RC3 types ‘AB’ turn out to be unbarred and RC3 bar classes ‘B’ and ‘AB’ have a significant overlap in e_{bar} . (6) Most (68% in *B* and 76% in *H*) bars have sizes below 5 kpc. Bar and disk sizes correlate, and the ratio (a_{bar}/R_{25}) lies primarily in the range 0.1 to 0.5. This suggests that the growth of bars and disks is intimately tied.

Subject headings: galaxies: fundamental parameters — galaxies: structure — galaxies: kinematics and dynamics — galaxies: evolution

1. INTRODUCTION

Stellar bars are recognized as the most important internal factor that redistributes the angular momentum of the baryonic and dark matter components of disk galaxies (e.g., Weinberg 1985; Debattista & Sellwood 1998, 2000; Athanassoula 2002; Berentzen, Shlosman, & Jogee 2006), thereby driving their dynamical and secular evolution. Bars efficiently drive gas from the outer disk to the central few hundred parsecs and are observed to feed central starbursts in local galaxies (Elmegreen 1994; Knapen et al. 1995; Hunt & Malakan 1999; Jogee et al. 1999; Jogee, Scoville, & Kenney 2005). It remains a matter of contention whether large-scale bars relate to AGN activity in galaxies, given the reduction by several orders of magnitude needed in the specific angular momentum of gas before it can feed a central black hole, and conflicting observational results (see review by Jogee 2006 and references therein; also Mulchaey & Regan 1997; Knapen et al. 2000; Laine et al. 2002; Laurikainen et al. 2004). In several galaxies, bar-driven gas inflows appear intimately tied to the formation of disky, high v/σ stellar components in the inner kpc, or ‘pseudobulges’ (Kormendy 1993; Jogee 1999; review by Kormendy & Kennicutt 2004; Jogee, Scoville, & Kenney 2005; Athanassoula 2005). Furthermore, the orbital structure of bars can lead to the ob-

served peanut-shaped and boxy bulges in inclined galaxies (Combes et al. 1990; Pfenniger & Norman 1990; Bureau & Athanassoula 2005; Athanassoula 2005; Martinez-Valpuesta et al. 2006; Debattista et al. 2006).

Earlier *Hubble Space Telescope* (*HST*) studies at optical wavelengths (e.g., Abraham et al. 1999) reported a paucity of stellar bars and a sharply declining optical bar fraction at intermediate redshifts $z > 0.5$. Studies at near-infrared (NIR) wavelengths also found a low bar fraction, but the authors rightly concluded that the large effective point spread functions (PSFs) of the NIR camera only allowed the detection of large bars whose semi-major axes exceeded $0.9''$, corresponding to 7.2 kpc^2 at $z \sim 1.0$ (Sheth et al. 2003). Recent works based on large optical surveys have now demonstrated the abundance of bars at intermediate redshifts $z \sim 0.2$ – 1.0 , corresponding to lookback times of 3–8 Gyr (Elmegreen et al. 2004; Jogee et al. 2004; Zheng et al. 2005; Sheth et al. in preparation). The fundamental issue of how robust bars are, and the associated implications for bar-driven evolution in disks over the last 10 Gyr, remains open (e.g., Jogee et al. 2004; Shen & Sellwood 2004; Athanassoula, Lambert, & Dehnen 2005; Bournaud et al. 2005; Berentzen, Shlosman, & Jogee 2006; Berentzen & Shlosman 2006; Martinez-Valpuesta et al. 2006; Debattista et al. 2006).

In order to put bars in a cosmological context, it now

¹ Department of Astronomy, University of Texas at Austin, 1 University Station C1400, Austin, TX 78712-0259

² We assume in this paper a flat cosmology with $\Omega_M = 1 - \Omega_\Lambda = 0.3$ and $H_0 = 70 \text{ km s}^{-1} \text{ Mpc}^{-1}$.

behoves us to characterize the frequency and impact of bars by applying the *same quantitative* methods to large samples at $z \sim 0$ and at higher redshifts. Spurred by these considerations, we characterize in this paper the frequency and structural properties of bars in the local Universe at optical and NIR wavelengths, by ellipse-fitting the B and H images of the OSU Bright Spiral Galaxy Survey (OSUBSGS; Eskridge et al. 2002) of 180 spirals. The first goal of this study is to provide *quantitative* characterizations of the bar fraction f_{bar} (defined as the fraction of disk galaxies that are barred) and structural properties (sizes, ellipticities, etc.) of bars at $z \sim 0$, as a function of wavelength, Hubble types, and host galaxy properties. Furthermore, with the advent of high redshift *HST* surveys, such as the Tadpole field (Tran et al. 2003), the Galaxy Evolution from Morphology and SEDs (GEMS; Rix et al. 2004), the Great Observatories Origins Deep Survey (GOODS; Giavalisco et al. 2004), and COSMOS (Scoville et al. 2006), which trace bars in the rest-frame optical band out to $z \sim 1$, it becomes increasingly important to provide a reference baseline for bars at $z \sim 0$ in the optical band. Thus, a second goal of our study is to provide a *rest-frame optical* $z \sim 0$ point for bars based on ellipse fits, in order to directly compare with studies of intermediate-redshift bars (Jogee et al. 2004; Elmegreen et al. 2004; Zheng et al. 2005; Sheth et al. in preparation) that also use ellipse fits. In particular, we use in this paper the same procedure of ellipse fits (§ 3.1) and the same quantitative characterizations (§ 3.3) of bars that were applied by Jogee et al. (2004) to bars at intermediate redshifts ($z \sim 0.2$ – 1.0) in the GEMS survey.

Several studies have used the OSUBSGS to gauge bars in the local Universe (e.g., Eskridge et al. 2000; Block et al. 2002; Whyte et al. 2002; Buta et al. 2005), but they differ significantly from our study and cannot meet our two goals. Eskridge et al. (2000) visually classified bars in the H band, and in the B band, they used the Third Reference Catalog of Bright Galaxies (de Vaucouleurs et al. 1991; hereafter RC3) visual bar classes. Such visual classifications form an invaluable first step, but by definition, are subjective and difficult to compare with results from other studies. Block et al. (2002) and later Buta et al. (2005) applied the gravitational torque Q_b method, based on Fourier amplitudes, to H -band images of 163 and 147 OSUBSGS galaxies, respectively. This quantitative method is less subjective than visual classification, but the results of Block et al. (2002) and Buta et al. (2005) cannot be compared to intermediate redshift studies for two reasons. First, the latter studies were based on the *HST* Advanced Camera for Surveys (ACS) data and trace the rest-frame optical properties of bars, while Block et al. (2002) and Buta et al. (2005) deal with the rest-frame NIR. Second, it is non-trivial to derive Q_b for intermediate-redshift galaxies because of resolution and signal-to-noise limitations. Whyte et al. (2002) fitted ellipses to B -band images of only 89 of the 180 OSUBSGS galaxies, and do not provide a distribution of bar properties as a function of Hubble type. Our present study complements these existing studies by ellipse fitting B -band and H -band images of all 180 OSUBSGS galaxies, and performing a comprehensive, statistically significant analysis of barred galaxies in the local Universe. It complements the ongoing analysis

(Barazza, Jogee, & Marinova 2006) of local bars based on a sample of 5000 galaxies in the Sloan Digitized Sky Survey (SDSS).

The outline of this paper is as follows. § 2 discusses the sample selection based on the OSUBSGS survey (Eskridge et al. 2002). § 3 describes the ellipse-fitting method, the criteria used for identifying bars, and deprojection of images and profiles to face-on. In § 4.1–4.4, we present results on the bar fraction at $z \sim 0$, its dependence on Hubble type, the distribution of bar sizes and strengths as characterized by ellipse-fitting, and the variation of bar properties along the Hubble sequence. Results are presented both before and after deprojection to face-on. In § 4.5, we present a first-order comparison of the bar fraction and properties at $z \sim 0$ from OSUBSGS to those derived at $z \sim 0.2$ – 1.0 or lookback times of 3–8 Gyr from GEMS (Jogee et al. 2004) and the Tadpole field (Elmegreen et al. 2004). In § 4.6, we discuss the constraints set by our results for theoretical models addressing the robustness of bars, and the assembly of the Hubble sequence over cosmological times. § 5 presents the summary and conclusions.

This paper is the first in a series of three based on the OSUBSGS. Paper II (Marinova et al. in prep) will address the bulge properties and activity of barred and unbarred galaxies in the OSUBSGS sample. In paper III, we will present simulations that artificially redshift the rest-frame optical and NIR images of the local OSUBSGS sample out to $z \sim 1$ – 2 , in order to assess the impact of redshift-dependent systematic effects on the recovery rate of bars in surveys conducted by current and future facilities in the optical and IR, such as the planned Wide Field Camera 3 (WFC3) and the James Webb Space Telescopes (JWST).

2. DATA AND SAMPLE

The OSUBSGS targets local spiral galaxies that are taken from the RC3 catalog and chosen to represent the bright disk galaxy population in the local universe (Eskridge et al. 2002). The galaxies are selected using the following criteria: RC3 type of S0/a or later, ($0 \leq T \leq 9$), $M_B < 12$, $D_{25} < 6'.5$, and $-80^\circ < \delta < +50^\circ$ (Eskridge et al. 2002), and are imaged in the B , V , R , H , J , and K bands. The B and H images of 182 OSUBSGS galaxies are available as part of a public data release (Eskridge et al. 2002). Our starting sample (sample S1) consists of the afore-mentioned 182 OSUBSGS galaxies with B and/or H images. After discarding galaxies (2 galaxies or 1% of sample S1) that do not have images in both the B and H bands, we are left with sample S2 of 180 galaxies imaged in both bands. This constitutes the sample of galaxies to which we fitted ellipses in order to characterize bars and disks, as outlined in § 3.

3. METHOD FOR CHARACTERIZING BARS AND DISKS

We adopt the widely used procedure of characterizing bars and disks in galaxies via ellipse fits (e.g., Wozniak et al. 1995, Friedli et al. 1996; Regan et al. 1997; Mulchaey & Regan 1997; Jogee et al. 1999, 2002a,b, 2004; Knapen et al. 2000; Laine et al. 2002; Sheth et al. 2003; Elmegreen et al. 2004), as described in detail in § 3.1. Our analysis procedure is schematically illustrated in Figure 1 and described in sections 3.1 to 3.4.

3.1. Ellipse Fitting

We start with the sample S2 of 180 galaxies imaged in both the B and H bands (Fig. 1). We first remove stars from the B - and H -band images of each galaxy by replacing them with the average of the sky background using a circular aperture. We then find the center of the galaxy using the IRAF routine ‘imcenter’. We determine a maximum galaxy semi-major axis length (a_{\max}) out to which ellipses will be fitted in each image by finding out where the galaxy isophotes reach the sky level.

We then use the standard IRAF task ‘ellipse’ to fit ellipses to each image out to a_{\max} . We employ an iterative wrapper developed by Jogee et al. (2004) to run ‘ellipse’ up to to 300 times for each object in order to get a good fit across the whole galaxy. A successful fit is one where the routine is able to fit an ellipse at each radial increment from the center until it reaches a_{\max} . When using the iraf task ‘ellipse’ for ellipse fits, the goodness of the best fit is measured by four harmonic amplitudes (A3, A4, B3, B4), which describe by how much the actual isophote differs from the best-fitting ellipse (e.g., Jedrzejewski 1987). We have inspected plots of these residuals for representative strongly and weakly barred galaxies (e.g., NGC 4314, NGC 613, NGC 1187, NGC 0210, NGC 1300, NGC 7479, NGC 5701, NGC 4643, NGC 4548, NGC 4450, NGC 3681, NGC 3275, NGC 1703, and NGC 1358). We find that the A3 and B3 residuals are small, typically on the order of a few percent. Values for the A4 and B4 residuals typically range from 2% to 10%, and do not exceed 15%.

From the final fit for each galaxy, we generate radial profiles of surface brightness (SB), ellipticity (e), and position angle (PA). The fitted ellipses are over-plotted onto the galaxy images to generate overlays. Examples of the radial plots and overlays are shown in Figures 2, 4, and 5. For each galaxy, an interactive visualization tool (Jogee et al. 2004) is used to display both the radial profile and the overlays in order to perform an extra inspection of the fits.

Of the 180 galaxies in sample S2, 179 (99%) and 169 (94%) were successfully fitted in the H and B band, respectively. Of the 11 galaxies that could not be fitted in the B band, five had strong morphological distortions and seem to be interacting; one had a very bright, saturated star with leakage; and five had no clearly defined center. The latter five galaxies were all of later Hubble type (Sbc and Sc), and had very flat or irregular surface brightness profiles in the B band. Further analyses to characterize inclined, unbarred, and barred disks in § 3.2 were then restricted to the sample S3 of 169 galaxies with successful fits in both the B and H bands (Fig. 1).

3.2. Identifying and excluding highly inclined spirals

For sample S3, we use the B -band images, rather than the H -band images, to identify and characterize the outer disk because the former are deeper and trace the disk farther out. From the radial profiles generated by ellipse-fitting the B -band image, we measure the ellipticity (e_{disk}) and PA (PA_{disk}) of the outer disk. The outer disk inclination, i , is derived from e_{disk} using $\cos(i) = (1 - e_{\text{disk}})$. Of the 169 galaxies in sample S3, we find 33 (20%) galaxies with disk inclination $i > 60^\circ$ and classify them as ‘inclined’. They are listed in the lower part of Table 1. Figure 2 shows an example of the B -band radial profile and ellipse

overlays for an inclined galaxy.

We only use the final sample S4 (Fig. 1) of 136 moderately inclined ($i < 60^\circ$) spirals to further characterize the properties of bars (e.g., size, ellipticity, frequency) and disks in § 3.3–3.4. Such an inclination cutoff is routinely applied in morphological studies because projection effects make it very difficult to reliably trace structural features in a galaxy that is close to edge-on. The exclusion of highly inclined galaxies does not bias the distribution of Hubble types, as shown in Figure 3a, where the Hubble types of samples S3 and S4 are compared. The absolute V -band magnitudes (M_V) of both sample S3 and S4 cover the range -18 to -23, with most galaxies lying in the range $M_V \sim -20$ to -22 (Fig. 3b).

3.3. Characterizing bars and disks before deprojection

In § 3.4, we use the *deprojected* radial profiles of (SB, e , PA) to characterize the intrinsic properties of bars and disks in sample S4. However, we also decide to first perform the analysis on the *observed* radial profiles *before* deprojecting them to face-on. There are several reasons for this dual approach of deriving bar properties both before and after deprojection. First, it is useful to have bar properties (e.g., frequency, strength as characterized by ellipse-fitting, size) prior to deprojection to compare directly to studies at intermediate redshifts (Jogee et al. 2004, Elmegreen et al. 2004, Zheng et al. 2005), where deprojection is not done for several reasons, including the difficulty in accurately measuring the PA of the line of nodes and the inclination of the outer disk in noisy images of distant galaxies. Second, by having bar properties both before and after deprojection, we are able to assess whether deprojection makes a substantial difference to the statistical distributions of bar properties. A large difference would raise concerns for intermediate redshift studies or even for large nearby studies where deprojection is often not carried out.

For sample S4, we use the observed radial profiles of (SB, e , PA) and the ellipse overlays to classify galaxies as ‘unbarred’ (Fig. 4) or ‘barred’ (Fig. 5), according to the following quantitative criteria. A galaxy is classified as barred if the radial variation of ellipticity and PA follows the behavior that is expected based on the dominant orbits of a barred potential. Specifically the following conditions must be satisfied before a galaxy is deemed to be barred: (1) The ellipticity, e , increases steadily to a global maximum, e_{bar} , greater than 0.25, while the PA value remains constant (within 10°). This criterion is based on the fact that the main bar-supporting orbits, namely the ‘ x_1 ’ family of orbits, can be modeled by concentric ellipses with a constant PA as a function of radius in the bar region (Athanasoula 1992a). The requirement that the PA must remain constant in the bar region is important for excluding other spurious elliptical features that may mimic a bar signature in their ellipticity profile. (2) Then, at the transition from the bar to the disk region, the ellipticity, e , must drop by at least 0.1, and the PA usually changes. This criterion is justified by the fact that we expect a transition from the highly eccentric x_1 orbits near the bar end to the more circular orbits in the disk. We also note that the drop in ellipticity by 0.1 at the transition from bar to disk has been shown to work well in identifying bars (e.g.,

Knapen et al. 2000; Laine et al. 2002; Jogee et al. 2002a, 2002b, 2004).

What are the limitations of criteria (1) and (2) in identifying bars? We note that the ‘constant PA’ criterion that we use to identify bars may cause us to miss some weak bars at optical wavelengths due to the following reason. In weak bars, the shock loci and corresponding dust lanes on the leading edge of the bar are curved (Athanasoula 1992b). In optical images of weak bars, these curved dust lanes may cause the PA to twist or vary slightly along the bar, thereby preventing the ‘constant PA’ criterion from being met. In the case of very strong bars, the ‘constant PA’ criterion is a good one and isophotal twist is not an issue, because such bars have strong shocks and straight dust lanes along their leading edges (Athanasoula 1992b). In order to gauge how many bars we might be missing because of the ‘constant PA’ criterion, we identify galaxies that show a PA twist accompanied by an ellipticity maximum. It turns out that only a small fraction ($\sim 7\%$) of galaxies show this effect.

We also note that criterion (1) requires the peak ellipticity (e_{bar}) over the PA plateau to be greater than 0.25 before we call a feature a bar. We picked 0.25 for the practical reason that structures with lower ellipticities are quite round and not always readily distinguishable from disks. Nonetheless, one may be tempted to ask whether we would find more bars if this arbitrary limit of 0.25 were to be lowered, and whether there is a population of low-ellipticity (e.g., $e_{\text{bar}} \sim 0.10\text{--}0.25$) bars that we might miss. We investigated this question using the OSUBSGS sample, and find that there is no increase in the number of bars if the limiting value for e_{bar} in criterion (1) were to be lowered from 0.25 to 0.10. The reason for this becomes clear later, in Figure 13, which shows that the number of bars already starts to drop rapidly for ellipticities below 0.40, such that by the time we reach e_{bar} of 0.25, we are already probing the tail end of bar distributions.

In addition to classifying galaxies as ‘barred’ and ‘unbarred’, we also use the radial profiles to derive the structural properties of the bar and disk. Specifically, for all galaxies, we measure the ellipticity, PA, and semi-major axis of the outer disk (e_{disk} , PA_{disk} , a_{disk}). For galaxies classified as ‘barred’, we also measure the maximum ellipticity (e_{bar}), the PA, and the semi-major axis of the bar. We will discuss in § 4.3 how the maximum bar ellipticity (e_{bar}) constrains the bar strength. Here, we discuss the question of how to locate the end of the bar in order to measure the bar semi-major axis. There has been some discussion in the literature as to whether the bar end should be defined as the radius (a_{bar}) where the bar ellipticity is a maximum, or as the radius where the PA changes abruptly at the transition from the bar to the disk. From a theoretical perspective, several early simulations (e.g., Athanasoula 1992a; O’Neill & Dubinski 2003) show that the definition of bar length based on ‘peak ellipticity’ can underestimate the true extent of the bar. Recently, Martinez-Valpuesta, Shlosman, & Heller (2006) have performed a systematic study of the radius (a_{bar}) of maximum bar ellipticity and the bar length. They show that there is a very good correspondence between two independent methods to determine the bar size: ellipse fitting and orbital analysis. The orbital analysis has involved finding

the largest (Jacobi) energy x_1 orbit in the bar that is still stable. The ellipse fitting becomes better if the size of the bar is given by the radius where the ellipticity declines by 15% from its maximal value.

In his empirical study of bar sizes using ellipse fits, Erwin (2005) argues that using the PA signature to define the bar size provides an upper limit, and that the two measures of bar length are very well correlated. However, he finds that it is harder to unambiguously measure the bar size from the PA criterion and that the definition of bar size based on peak ellipticity is more readily applied consistently to a large number of different galaxy morphologies (Erwin 2005). In this study, we have adopted the first approach. We use the semi major axis (a_{bar}) where the maximum bar ellipticity occurs as a measure of the bar length. We caution that this may underestimate the bar length in some galaxies. However, a visual comparison of a_{bar} with the images of our galaxies suggests that a_{bar} does a reasonable job in most cases.

3.4. Characterizing bars and disks after deprojection

For sample S4, we use the inclination, i , and the PA of the outer disk (determined in § 3.2) to *analytically* deproject the observed H and B band radial profiles of (e , PA) to face-on. We perform the analytical deprojection using a code developed by Laine et al. (2002) and used previously in Laine et al. (2002) and Jogee et al. (2002a,b). It should be noted that the deprojection formula used in the code only strictly applies to infinitesimally thin structures, and may be inaccurate near the galaxy center in the vicinity of the bulge. However, it is a reasonable approximation in the region of interest where large-scale bars reside. Figure 6 shows an example of the deprojected radial profiles of NGC 4548 in the B and H bands overlaid on the observed profiles.

We note that the process of analytically deprojecting the radial profiles to face-on after ellipse-fitting the observed (i.e, un-deprojected) images is analogous to the process of first deprojecting the observed images to face-on, and then ellipse-fitting the deprojected images in order to generate face-on radial profiles. The two methods should yield the same results unless the images are very noisy. We verified this expectation with the following steps. (1) We deproject the images of several galaxies using the Multi-channel Image Reconstruction, Image Analysis and Display (MIRIAD) routine ‘deproject’. The routine takes as input the observed image, the galaxy center, the inclination i and PA of the outer disk, and outputs the deprojected image; (2) We then fit ellipses to these deprojected images using the procedure outlined in § 3.1, and generate face-on radial profiles of SB, e , and PA; (3) These face-on radial profiles generated from the deprojected images, are compared with the deprojected radial profiles derived analytically from the the observed profile. There is good agreement in all cases, showing that we are not noise limited.

This is illustrated in Figure 7 for the B band image of NGC 4548. The observed and deprojected images are shown in the left panel. In the right panel, three radial profiles are plotted: the observed radial profile derived by fitting ellipses to the observed image is plotted as stars; the deprojected radial profile derived analytically from the ob-

served profile is plotted as squares; and the face-on radial profile derived by fitting ellipses to the deprojected image is plotted as triangles. There is good agreement between the squares and the triangles.

The deprojected profiles provide an accurate characterization of the ‘intrinsic’ or face-on properties of disks and bars. For all galaxies in S4, we therefore use the analytically deprojected B and H radial profiles to classify galaxies as ‘barred’ or ‘unbarred’, according to the criteria outlined in § 3.3. We also re-measure the bar ellipticity (e_{bar}), semi-major axis (a_{bar}), and disk size a_{disk} from the deprojected radial profile. In the rest of this paper, many of these deprojected quantities will be compared to those derived before deprojection (§ 3.3) in order to gauge the impact of deprojection.

4. RESULTS AND DISCUSSIONS

4.1. The optical and NIR bar fraction at $z \sim 0$

Table 2 and Figure 8 show the bar fraction (defined as the fraction of spiral galaxies that are barred) for the B and H bands, both before (§ 3.3) and after deprojection (§ 3.4). The results are based on sample S4 of 136 moderately inclined ($i < 60^\circ$) spirals (§ 3.2). The sample is dominated by galaxies with $M_V \sim -20$ to -22 . We find a deprojected bar fraction of 60% in the H band and a lower fraction of 44% in the B -band images, which likely miss bars obscured by dust and star formation. Our results that 60% of spirals are barred in the infrared confirms the preponderance of bars among spirals in the local Universe.

Our H -band bar fraction of $\sim 60\%$ is in agreement with the NIR bar fraction of 59% (Menendez-Delmestre et al. 2006) based on 2MASS. It is also consistent, within a margin of 12%, with the results of Eskridge et al. (2000), who visually inspected the OSUBSGS H -band images and reported an overall H -band bar fraction of 72%, with 56% of spirals hosting ‘strong’ bars and 16% hosting ‘weak’ bars. Why is there a 12% deviation? The Eskridge et al. (2000) paper does not give ‘barred’ or ‘unbarred’ classifications for individual galaxies, so we can not make a case by case comparison with that study. However, in a subsequent paper, Eskridge et al. (2002) give visual classifications of individual galaxies as barred or unbarred, and classify barred systems as ‘SB’ (strongly barred) and ‘SAB’ (weakly barred). We find that our classifications as barred or unbarred disagree on 25 galaxies in the B band ($\sim 18\%$ of sample S4), and 23 galaxies in the H band ($\sim 17\%$ of sample S4). Of the galaxies in the B band and H band where we differ, we find that the majority (15 of the 25 galaxies in the B band, and 11 of the 23 galaxies in the H band) are classified as ‘SAB’ (weakly barred) by Eskridge et al. (2002). We conclude that, as might be intuitively expected, the differences between visual and quantitative classifications of bars are strongest for systems that visually appear as ‘weakly barred’.

How does our study compare with other quantitative studies? We find that our reported H -band bar fraction of 60% agrees with that of Laurikainen et al. (2004), who used Fourier modes and the Q_b method for 158 galaxies in the OSUBSGS sample and 22 2MASS galaxies. Laurikainen et al. (2004) find a NIR bar fraction of 62% for galaxies with $i < 60^\circ$. We present a more detailed comparison of our bar ellipticity and fraction with other studies

in § 4.3.

Another important result is that deprojection does not make any significant changes to the global bar fraction, when dealing with the fairly large OSUBSGS sample. As shown by Table 2 and Figure 8, the B - and H -band bar fractions are 45% and 58% before deprojection, and change by only a factor of 0.97 and 1.03, respectively, after deprojection. We suggest several reasons for the small impact of projection effects. First, this study uses only moderately inclined ($i < 60^\circ$) galaxies where projection effects are less severe than in highly inclined systems. Second, projection effects produce large changes in the morphology of a galaxy only when the disk inclination, i , is significant *and* the difference in PA between the bar and the disk major axes is close to 90° . From a statistical point of view, these two conditions are unlikely to occur simultaneously in a dominant fraction of the sample. These arguments are supported by Figures 9a and 9b, which show that the galaxy classes assigned prior to deprojection are in no way biased by the galaxy inclination, i : both barred and unbarred galaxies span a similar range in i . Furthermore, even the bar ellipticity e_{bar} measured before deprojection is uncorrelated with i (Figs. 9c and 9d).

The fact that the bar fraction in large samples is similar before and after deprojection is encouraging for large studies of bars at intermediate redshift (e.g., Jogee et al. 2004, Elmegreen et al. 2004, Zheng et al. 2005), where deprojection is not done because of the difficulty in accurately measuring the PA of the line of nodes and the inclination of the outer disk in noisy images of distant galaxies.

4.2. Sizes of bars and disks at $z \sim 0$

As outlined in § 3.1, we use the semi major axis a_{bar} , where the bar ellipticity is a maximum, as a measure of the bar length. We caution that this may underestimate the bar length in some galaxies. However, a visual comparison of a_{bar} with the images of our galaxies suggests that a_{bar} does a reasonable job in most cases.

The distributions of bar sizes or semi-major axes (a_{bar}) before and after deprojection are shown for the B and H bands in Figure 10. Some bars do appear larger after deprojection, but from a statistical point of view, deprojection does not have a substantial effect on the bar size distribution. For example, the mean bar size in the H band before deprojection is 3.4 kpc and after deprojection it is 4.0 kpc. Sizes of large-scale bars in the local Universe lie in the range ~ 1 to 14 kpc, with most (68% in B and 76% in H) bars having $a_{\text{bar}} \leq 5$ kpc, and $\sim 50\%$ of them clustering with a_{bar} in the range 2 to 5 kpc. If such a distribution of bar sizes is present at a redshift $z \sim 1$, where $1''$ corresponds to 8.0 kpc, then only observations with angular resolutions superior to $0''.3$ can adequately resolve the majority of bars. This is relevant for assessing the relative effectiveness of current NIR capabilities, such as NICMOS, and those of future planned missions, such as WFC3, in detecting high redshift bars in the NIR band over wide fields.

In Figure 11, we plot the bar size versus the disk size before and after deprojection. The bar size is measured from the H band, whose low extinction enables more accurate measurement than in the optical. The disk is measured from the B -band image, which is deeper than the H band

and traces the disk further out (§ 3.2). Both before and after deprojection, we find that bar and disk sizes are correlated with an average slope of ~ 0.9 , albeit with a large scatter of several kpc in bar size at a given disk size.

Figure 12 shows the observed bar semi-major axis distribution normalized to R_{25} (the radius in arcseconds of the isophote, where the surface brightness equals 25 mag arcsec $^{-2}$) of the disk. R_{25} values are obtained from the Nearby Bright Galaxies Catalogue (Tully 1988; hereafter NBG), except for NGC 6753, 6782, 5078, 6907, 7814, and ESO 142-19, which are from the RC3. The ratio (a_{bar}/R_{25}) lies primarily in the range 0.1 to 0.5 in both the H and B bands (Fig. 12). Only a minority of galaxies have larger values out to 0.95.

These results are consistent with several smaller earlier studies. Laine et al. (2002) find that the sizes of primary bars correlate with the host galaxy sizes and the (a_{bar}/R_{25}) ratio lies primarily in the range 0.1 to 0.5. Menendez-Delmestre et al. (2004) find an average (a_{bar}/R_{25}) ratio of 0.35, on the basis of ellipse fits of 134 2MASS galaxies. In his study of bar lengths, based on ellipse fits of R -band images of 65 local early-type S0-Sab galaxies, Erwin (2005) finds a similar mean (a_{bar}/R_{25}) ratio of 0.38 and reports a correlation between bar size and disk size.

What do these results imply? From a theoretical standpoint, the size of the bar (a_{bar}) depends on the concentration of matter in the disk and the distribution of resonant material that can absorb angular momentum from the bar (Athanasoula 2003). Furthermore, the prevalence of chaotic orbits between the 4:1 and the corotation resonance (CR) would naturally lead bars to end somewhere between the two resonances. If bars end very near the CR as is found observationally (e.g., Merrifield & Kuijken 1995; Debattista et al. 2002; Aguerri et al. 2003), then our result that (a_{bar}/R_{25}) is generally well below 1.0 suggests that the CR of disk galaxies lies well inside their R_{25} radius. Furthermore, the correlation between bar and disk sizes and the narrow range in (a_{bar}/R_{25}) suggests that the growths of the bar and disk may be intimately tied.

4.3. Distribution of bar strengths as characterized by e_{bar} at $z \sim 0$

The term ‘bar strength’ is not well defined in the literature. Various measures of bar strength are used and each measure has some benefits and trade-offs. These measures include the Q_b method (Block et al. 2002; Buta et al. 2003; Buta et al. 2005), the maximum ellipticity of the bar, bar/interbar contrasts, Fourier decomposition techniques (Elmegreen & Elmegreen 1985; Elmegreen et al. 1996), and visual estimates of strength (e.g., Martin 1995; Eskridge et al. 2000, 2002) gauged via eyeball inspection of images.

The Q_b method (Block et al. 2002; Buta et al. 2003; Buta et al. 2005) directly measures the gravitational torque exerted by the bar, but it measures the torque at only one point along the bar. The Q_b method depends on the scale height of the disk and the ability to derive a reliable model for the potential using images. It is hard to apply this method to a large number of intermediate redshift galaxies due to resolution and signal-to-noise limitations. In the bar/interbar contrast method

used by Elmegreen & Elmegreen (1985) and Elmegreen et al. (1996), the bar strength is characterized by the ratio of the peak surface brightness in the bar region to the minimum surface brightness in the interbar region. The Fourier decomposition method also used by Elmegreen & Elmegreen (1985) and Elmegreen et al. (1996) is similar to the Q_b method. It characterizes bar strength by measuring the relative amplitudes of the Fourier components of the bar. The maximum amplitude of the $m=2$ mode determines the strength of a bar.

In studies where ellipse fits are used to characterize bars, the maximum ellipticity of the bar (e_{bar}) is used as a measure of bar strength (e.g., Athanasoula 1992a; Martin 1995; Wozniak et al. 1995; Jogee et al. 1999, 2002a,b; Knapen et al. 2000; Laine et al. 2002). One advantage of this approach is that the bar ellipticity can be estimated without making any assumptions about the mass to light ratio of the galaxy or its scale height. It can also be applied to local galaxies as well as galaxies out to intermediate redshifts ($z \sim 0.2$ –1.0; Jogee et al. 2004, Elmegreen et al. 2004). There are also several theoretical reasons that support the use of the maximum bar ellipticity as a measure of bar strength. Shen & Sellwood (2004) compare bar strength in N-body simulations, as characterized by the $m = 2$ Fourier components and the peak ellipticity. They find that the ellipticity is very well correlated to bar strength estimator A , where A is the relative amplitude of the bisymmetric ($m = 2$) Fourier component of the mass density averaged over a certain inner radial range where the bar dominates. In addition, from an observational standpoint, Laurikainen et al. (2002) find that, on average, the gravitational torque, Q_b , and e_{bar} are correlated for $e_{\text{bar}} \leq 0.6$. For higher e_{bar} values, the relation appears to flatten out although the small number of galaxies precludes a firm conclusion.

Nonetheless, if we deem that a measure of bar strength should give an indication of the gas inflow rate that a bar drives via gravitational torques, then the maximum ellipticity of the bar (e_{bar}) is only a *partial* measure of the bar strength. Both the mass and shape of the bar influence the magnitude of the gravitational torque at each point along the bar. The peak bar ellipticity describes the shape of the bar, but does not directly measure its mass or luminosity. While bearing this caveat in mind, we use the maximum bar ellipticity e_{bar} as a partial measure of the bar strength in this study.

Figure 13 shows the observed and deprojected distributions of bar strength as characterized by e_{bar} from ellipse fits in the B (Figs. 13a,c) and H bands (Figs. 13b,d). It is striking that only a very small proportion (7% in B ; 10% in H) of bars are very weak with $0.25 \leq e_{\text{bar}} \leq 0.40$, while the majority of bars (70% in B ; 71% in H) have moderate to high strengths as characterized by e_{bar} , with $0.50 \leq e_{\text{bar}} \leq 0.75$. This point is further illustrated in Figure 14, which is a generalized plot of the fraction of disks with ‘strong’ and ‘weak’ bars. It shows how the fraction of spiral galaxies that host bars with ellipticities ($e_{\text{bar}} > e_1$) changes as we vary e_1 . As we increase e_1 from 0.35 to 0.45, 0.55, and 0.75, the deprojected bar fraction in the B band falls from 43% to 39%, 34%, and 7%, respectively. Correspondingly, the bar fraction in the H band falls from 59% to 47%, 30%, and 1%, respectively. The flattening

of the curve around $e_1 \sim 0.40$ shows that the majority of bars have e_{bar} above this value. This has implications for theoretical models that address the robustness of bars, and we refer the reader to § 4.6 for a discussion.

How do our results on bar strength as characterized by the maximum bar ellipticity e_{bar} from ellipse-fitting compare with those of Buta et al. (2005) who use the Q_b parameter? At first glance, the results may seem contradictory: they conclude that 40% of the galaxies in the OSUBSGS H band have ‘weakly barred’ or unbarred states ($Q_b \leq 0.1$), whereas we find that only 6% of galaxies have ‘weak’ bars with $0.25 \leq e_{\text{bar}} \leq 0.4$ in the H band after deprojection. However, it should be noted that Buta et al. (2005) group unbarred and weakly barred galaxies together. Their cited fraction of 40% for weak and unbarred states is, in fact, fully consistent with the fraction (46%) that we find when we group together unbarred galaxies (40%) and ‘weakly barred’ galaxies (6%).

How do the bar classes and bar strengths from ellipse-fits, as derived by our quantitative method (§ 3.3), compare with the RC3 bar classes based on visual inspection of optical B images (de Vaucouleurs et al. 1991)? The three RC3 visual bar classes, ‘A’, ‘AB’, and ‘B’ denote ‘unbarred’, ‘weakly barred’, and ‘strongly barred’ disks, respectively. Of the 42, 47, and 46 galaxies in our sample that have an RC3 bar class of ‘A’, ‘B’, and ‘AB’, respectively, our quantitative characterization (§ 3.3) shows that 5%, 85%, and 41% host bars in B -band images and 19%, 87%, and 65% host bars in H -band images. Clearly, only a small fraction (41% or 19/46) of galaxies with RC3 bar class ‘AB’ qualify as barred in B -band images, according to our quantitative criteria (§ 3.3). We visually inspected the remaining 27 galaxies that fail to qualify in order to investigate why they do not. We found that for 17 of them, we could not identify a bar feature in the B -band image, even by eye. For the remaining 10, we could visually see a somewhat elongated feature, but it does not satisfy the ellipticity and PA criteria outlined in § 3.3. Another interesting point highlighted by Figure 15 is that while the mean bar strength (as characterized by e_{bar}) is higher for RC3 visual class ‘B’ than for class ‘AB’, the two classes have significant overlap in the range $e_{\text{bar}} \sim 0.5$ – 0.7 . Thus, RC3 bar types should be used with caution and may be misleading.

It is also noteworthy that Figure 13 shows no evidence for bimodality in the distribution of bar strength, as characterized by e_{bar} from ellipse fits, in the B or H bands, in agreement with Buta et al. (2005). What about the bimodality claimed in earlier studies by Abraham & Merrifield (2000) and Whyte et al. (2002)? Both of these studies used the parameter f_{bar} to characterize the ellipticity of the most elliptical feature of a galaxy, and measure f_{bar} for both barred and unbarred galaxies. They report no bimodality in f_{bar} among barred galaxies, which is consistent with our findings that e_{bar} shows no bimodality among barred galaxies. The only bimodality that they report in f_{bar} is between barred and unbarred galaxies. It is unclear how robust this bimodality is since Whyte et al. (2002) report a bimodality that is much weaker than the one seen by Abraham & Merrifield (2000). The authors assigned this weakening to the larger sample size used by Whyte et al. (2002). At any rate, we cannot make any direct com-

parison with their bimodality results involving unbarred galaxies, since we measure e_{bar} in barred galaxies, but not in unbarred galaxies. The reason for this selective measurement is rooted in our rigorous approach for identifying a bar. In the study of Abraham & Merrifield (2000) and Whyte et al. (2002), a bar is simply considered as the innermost feature whose isophote has the highest ellipticity. In contrast, we use a rigorous approach for identifying a bar: we call a feature a bar only if its radial variation of ellipticity and PA follows the behavior expected based on the dominant orbits of a barred potential, as outlined in § 3.3. We measure the maximum bar ellipticity e_{bar} only for those features that qualify as a bar.

4.4. Bar fraction and ellipticity as a function of Hubble type at $z \sim 0$

Figure 16 shows how the fraction of barred disks varies across different Hubble types in sample S4. The Hubble types are taken from RC3 and the bins represent S0, Sa/Sab, Sb/Sbc, Sc/Sd, and Sd/Sm. We first note that the bar fraction in different RC3 Hubble types does not change significantly after deprojection, whether in the B (Fig. 16a vs. 16d) or H (Fig 16b vs. 16e) band images. This is again encouraging for large studies of bars at intermediate redshift (e.g., Jogee et al. 2004, Elmegreen et al. 2004, Zheng et al. 2005), where deprojection is not done for the reasons outlined in § 4.1.

In the B band, we find that the bar fraction is lower with respect to the H band by ~ 1.2 – 1.5 in SAs to Scs, and by ~ 2.5 in Sds/Sms (Fig. 16c,f). This is consistent with higher obscuration in dusty, gas-rich late types. Eskridge et al. (2000) also find that the increase in bar fraction from the B to H band is most significant for late-type galaxies.

How does the bar fraction vary across RC3 Hubble types? The number of galaxies involved are too small in the S0 and Sd/Sm bins for robust number statistics and we therefore restrict our analysis to types Sa to Scd. We conclude that the H -band bar fraction (Fig 16e) remains $\sim 60\%$ across RC3 Hubble types Sa to Scd. Our quantitative result based on 136 galaxies is consistent with the results based on ellipse fits of a much smaller sample (58 galaxies) by Knapen, Shlosman, & Peletier (2000), as well as with the qualitative results of Eskridge et al. (2000), who also report a constant NIR bar fraction as a function of RC3 Hubble types, based on visual inspection. The large H -band bar fraction of $\sim 60\%$ across different Hubble types implies that bars are ubiquitous in spirals across the entire Hubble sequence. Further implications are discussed in § 4.6.

How does the bar strength, as characterized by e_{bar} from ellipse-fitting, vary as a function of RC3 Hubble type? In the H band, the bar strength e_{bar} lies in the range 0.35–0.80, and shows no systematic variation across Hubble types Sa to Scd, either before (Fig. 17a) or after (Fig. 17b) deprojection. We note, however, that Buta et al. (2004) and Laurikainen et al. (2004) find that the Q_b and Q_g parameters tend to have lower values toward earlier-type galaxies. In order to understand this discrepancy, we first note that the Q_b and Q_g parameters measure the bar strength relative to the axisymmetric components, such as the disk and bulge. The lower Q_b and Q_g values in early type galaxies could reflect the fact that such galaxies have

stronger axisymmetric components, which make the relative strength of the bar lower, even if the bar was as strong or stronger intrinsically than those in later-type galaxies.

4.5. Comparison of optical properties of bars at $z \sim 0$ and at $z \sim 0.2-1.0$

Studies of bars at $z \sim 0.2-1.0$ (lookback times of 3–8 Gyr) based on *HST* ACS observations in the Tadpole field (Elmegreen et al. 2004), the GEMS and GOODS fields (Jogee et al. 2004), and COSMOS surveys (Sheth et al. in preparation) trace bars in the *rest-frame optical*. The reddest ACS filter F850LP has a pivot wavelength of 9103 Å, while the value for the F814W filter is 8064 Å. Over the redshift range $z \sim 0.2-1.0$, the rest-frame wavelength traced by the F850LP filter ranges from 7586 Å to 4550 Å, which corresponds to the *rest-frame optical R/I to V/B* bands. In order to avoid the pernicious effects of band-pass shifting, it is essential that ACS studies of bars at $z \sim 0.2-1.0$ compare their rest-frame optical results to the optical bar fraction at $z \sim 0$, rather than to the NIR bar fraction at $z \sim 0$. If the NIR $z \sim 0$ point is used for comparison (e.g. Menendez-Delmestre et al. 2006), it will lead to flawed conclusions because the NIR $z \sim 0$ bar fraction ($60\% \pm 6\%$) is significantly larger than the optical $z \sim 0$ bar fraction ($44\% \pm 6\%$), as reported in § 4.1. We therefore use the OSUBSGS optical bar fraction at $z \sim 0$ in the discussion below.

In the study of bars at $z \sim 0.2-1.0$, Jogee et al. (2004) ellipse fitted a sample of 1590 galaxies at $z \sim 0.2-1.0$, drawn from 25% of the GEMS survey area. Then they applied essential cutoffs in absolute magnitude, bar size, and bar ellipticity in order to ensure a complete sample, high spatial resolution, and reliable bar identification out to $z \sim 1$. In particular, in order to ensure that the sample of spiral galaxies is fairly complete out to $z \sim 0.9$, an absolute magnitude cutoff of $M_V < -19.3$ had to be applied. Secondly, at $z > 0.5$ (where $1''$ corresponds to scales > 6.2 kpc), the study could not efficiently resolve very small bars with semi-major axes $a < 1.5$ kpc, in agreement with Lisker et al. (2006). Thus, a cutoff of $a_{\text{bar}} \geq 1.5$ kpc is implicitly applied. Finally, the study only considered bars with moderate ellipticity $e_{\text{bar}} \geq 0.4$ because at intermediate redshifts, it becomes difficult to unambiguously identify and characterize bars with lower ellipticities. This is not a dramatic cutoff as most bars have $e_{\text{bar}} \geq 0.4$ (Fig. 13). After applying these cutoffs in absolute magnitude ($M_V < -19.3$), bar size ($a_{\text{bar}} \geq 1.5$ kpc), and bar ellipticity ($e_{\text{bar}} \geq 0.4$), Jogee et al. (2004) find a rest-frame optical bar fraction of $f_{\text{optical2}} \sim 30\% \pm 6\%$ $z \sim 0.2-1.0$. A constant and similar optical bar fraction (23% to 40%) out to $z \sim 1$ is also reported by Elmegreen et al. (2004).

In order to get a valid optical bar fraction for comparison at $z \sim 0$, we must apply the exact same cutoffs to the OSUBSGS optical data. We start with observed bar properties prior to deprojection from OSUBSGS because no deprojection was applied in any of the intermediate redshift studies (Jogee et al. 2004; Elmegreen et al. 2004; Zheng et al. 2005). With a cutoff of $M_V < -19.3$, the optical *B*-band bar fraction at $z \sim 0$ drops from 45% (61/136) to 43% (45/104). Applying a further cutoff of $a_{\text{bar}} \geq 1.5$ kpc makes it drop to 36% (37/104). Finally, a third cutoff of $e_{\text{bar}} \geq 0.4$ reduces the optical *B*-band bar fraction to

34% (35/104).

Thus, after the same cutoffs in absolute magnitude ($M_V < -19.3$), bar size ($a_{\text{bar}} \geq 1.5$ kpc), and bar ellipticity ($e_{\text{bar}} \geq 0.4$) are applied, a very good agreement ensues between the GEMS optical bar fraction at $z \sim 0.2-1.0$ ($f_{\text{optical2}} \sim 30\% \pm 6\%$) and the OSUBSGS optical *B*-band bar fraction at $z \sim 0$ ($f_{\text{optical3}} \sim 34\% \pm 6\%$). This agreement strongly suggests that the optical bar fraction in bright disks does not decline strongly with redshift. Such a decline would cause $f_{\text{optical2}} \ll f_{\text{optical3}}$ because the observed bar fraction would be lowered both by the intrinsic decline, and by systematic effects at intermediate redshifts, such as cosmological dimming, the loss of spatial resolution, and lower signal-to-noise.

However, our finding allows for models where the optical bar fraction is either constant, or rises with redshift. In the latter class of models, one can arrive at comparable values of f_{optical2} and f_{optical3} only if the intrinsic increase in bar fraction with redshift produced by the model is compensated for by the ‘loss’ of bars due to systematic effects, such as cosmological dimming, and low signal-to-noise. In a forthcoming paper, we will assess the impact of such redshift-dependent systematic effects by artificially redshifting the OSUBSGS sample to $z \sim 1$, and repeating the bar characterizations. This will enable us to distinguish between the two classes of models.

4.6. Constraints on the robustness and evolution of bars

The robustness and lifetime of bars define some of the most fundamental issues in the evolution of bars, their impact on disk galaxies (§ 1) and the assembly of the Hubble sequence. In general terms, the evolution of a bar depends on the exchange of angular momentum between the stars in the bar and the other components of a galaxy, namely, the dark matter (DM) halo and the baryons (gas and stars) in the bulge and disk. Important factors influencing the bar include the triaxiality of the DM halo in which it lies (e.g., Berentzen, Shlosman, & Jogee 2006); the amount of angular momentum that the DM halo can absorb (Athanasoula 2003); the central mass concentrations (CMCs) present in the inner few hundred pc (e.g., Shen & Sellwood 2004; Athanasoula et al. 2005; Martínez-Valpuesta et al. 2006; Debattista et al. 2006); and the distribution and amount of gas in the disk (e.g. Shlosman & Noguchi 1993; Bournaud et al. 2002, 2005; Debattista et al. 2006). In this section, we compare our empirical results to different simulations in order to constrain theoretical scenarios. We note, however, that most simulations do not yet fully incorporate the effects of star formation and feedback, which can impact the evolution of the disk in important ways.

Dubinski (1994) showed that the triaxiality of DM halos is diluted by baryonic dissipation. Recent simulations by Berentzen, Shlosman, & Jogee (2006) find that bars embedded in triaxial non-rotating DM halos can only survive if the inner halo ellipticity is washed out. Otherwise, the interaction between the bar and the DM halo induces chaotic orbits and destroys the bar. In the present paper, our findings that the majority (60%) of spirals are barred in the infrared (§ 4.1), and that these bars have primarily moderate to high strengths, as characterized by the maximum bar ellipticity e_{bar} ($0.50 \leq e_{\text{bar}} \leq 0.80$; § 4.3),

suggest that DM halos of most present-day spirals are close to axisymmetric, with a maximum equatorial axial ratio of ~ 0.9 in potential. These limits may change slightly if one allows the DM halo to have a figure of rotation. These results are consistent with Kazantzidis et al. (2004), who find that in the very early stages of disk formation, the settling of the dissipative baryonic component within a triaxial halo strongly dilutes the triaxiality to such values. Berentzen & Shlosman (2006) also report that a growing disk is responsible for washing out the halo prolateness (in the disk plane) and for diluting its flatness over a period of time comparable to the disk growth.

The CMC typically refers to the mass present within the inner hundred or few hundred pc. A large or more centrally concentrated CMC can weaken a bar amplitude by changing the orbital structure of a barred potential and inducing chaotic orbits. Most recent simulations (e.g., Athanassoula et al. 2005; Shen & Sellwood 2004; Martinez-Valpuesta et al. 2006; Debattista et al. 2006) find that bars are more robust than previously thought: in order to produce any significant reduction in bar strength, the ratio $X_{\text{CMC}} \sim (M_{\text{CMC}}/M_{\text{disk}})$, where M_{CMC} is the mass of the CMC in the inner few hundred pc, and M_{disk} is the disk mass, must be very large, at least 10%. Such large values are only of academic interest and are not realized in present-day galaxies, as we discuss below.

In present-day galaxies, the components that contribute to the CMC in the inner few hundred pc consist of super-massive black holes (SMBHs) central dense stellar clusters, gaseous concentrations, and the inner parts of bulges. SMBHs have typical masses in the range 10^6 – $10^9 M_{\odot}$ and tend to scale as 0.001 of the bulge mass; gaseous concentrations range from 10^7 – $10^9 M_{\odot}$ in the central 500 to 1000 pc radius (e.g., Jogee et al. 2005); and central dense stellar clusters typically have masses in the range 10^6 – $10^8 M_{\odot}$. These components typically lead to X_{CMC} values that are much lower than 10%. This suggests that CMCs that exist in present-day galaxies are not large enough to produce any significant reduction in bar strength. Our results are consistent with these expectations and with simulations that support robust bars. We found that the majority ($\sim 71\%$ – 80%) of bars have moderate to high strengths, as characterized by e_{bar} from ellipse-fitting ($0.50 \leq e_{\text{bar}} \leq 0.80$). We also found that the bar fraction ($\sim 60\%$) and mean bar strength, as characterized by ellipse fits ($e_{\text{bar}} \sim 0.5$), is relatively constant across RC3 Hubble types Sa to Scd (§ 4.4), although the latter encompasses a wide range of gas mass fractions, CMC masses, and CMC components.

Gas can affect the formation and evolution of a bar in different ways, depending on its distribution and clumpiness. In the case of an unbarred disk, the accretion of cold gas makes the disk more massive, dynamically colder, and therefore more bar unstable (e.g., Bournaud et al. 2002). However, in the case of very gas-rich disks, the gas can become clumpy, and the effect of dynamical friction on massive gas clumps at low radii can heat the disk and prevent it from forming the bar (e.g., Shlosman & Noguchi 1993). In the case of a disk that is already barred, the bar exerts gravitational torques that drive gas located outside the corotation resonance (CR) outward, and drive gas located between the CR and inner Lindblad resonance

(ILR) inward. Most simulations to date (e.g., Debattista et al. 2006; Berentzen & Shlosman in preparation; Curir et al. 2006) suggest that gas inflows in present-day galaxies do not readily destroy bars. For instance, simulations (e.g., Debattista et al. 2006), can only destroy the bar when there are large gas inflows that build a very massive, soft CMC, of order 20% of the mass of the total baryonic (gas and stars) disk. Furthermore, the simulations also suggest that gas which sinks into the center can become bar supporting if it forms stars. As discussed above, CMCs as large as 10% or 20% are not realized in present-day galaxies and the simulations therefore imply that gas inflows in present-day galaxies do not readily destroy bars. In the very early Universe, if extreme gas inflows and extreme CMCs are realized, the evolution of bars might be different.

We note that simulations of bar-driven gas inflow by Bournaud et al. (2005) yield widely different predictions from those discussed above. The simulations of Bournaud et al. (2005) appear to destroy a bar even with a gas mass fraction (GMF) that is as low as 5% to 7%. Here, the GMF is defined as the ratio of gas mass to the total mass of the stellar disk. A GMF of order 5% is easily met in present-day galaxies and these simulations would suggest, therefore, that strong bars in present-day galaxies are easily destroyed by bar-driven gas inflows (Bournaud et al. 2005). There is clearly a stark difference between the predictions of these simulations and the ones outlined in the previous paragraph. Part of the reason why the simulations yield such different results might lie in the way the DM halo is modeled and the assumed ratio of DM halo mass to disk mass. The DM halo is live and dominates over the disk mass in Debattista et al. (2006), while it is rigid and less massive than the disk in Bournaud et al. (2005).

What do our observational results suggest? We found that at $z \sim 0$, only a small fraction ($\sim 7\%$ – 10%) of bars are very weak ($0.25 \leq e_{\text{bar}} \leq 0.40$), while the majority ($\sim 71\%$ – 80%) of bars have moderate to high strengths (as characterized by the maximum bar ellipticity e_{bar}), with $0.50 \leq e_{\text{bar}} \leq 0.80$. We also do not see any sign of bimodality in bar strength, as characterized by e_{bar} from ellipse fits. Finally, we found that the bar fraction ($\sim 60\%$) and mean bar ellipticity ($e_{\text{bar}} \sim 0.5$) is relatively constant across RC3 Hubble types Sa to Scd (§ 4.4), despite the wide variation in GMFs. Our results are easily reconciled with scenarios where bars in present-day moderately gas-rich galaxies remain strong under the effect of bar-driven gas inflows. Our results do not necessarily rule out models where bars are easily destroyed by bar-driven gas inflows. They do, however, imply that if such an easy destruction occurs, then there must be a very efficient mechanism that not only regenerates bars on a short timescale (e.g., Block et al. 2002; Bournaud et al. 2002), but is also very well tuned to the bar destruction rate so that it can reproduce the observed constant optical bar fraction in bright galaxies over the last 8 Gyr (Jogee et al. 2004; Elmegreen et al. 2004; § 4.5).

5. SUMMARY AND CONCLUSIONS

With the advent of high redshift *HST* surveys, such as the Tadpole Field, GEMS, GOODS, and COSMOS, which trace bars in the rest-frame optical band out to $z \sim 1$,

it becomes increasingly important to provide a reference baseline for bars at $z \sim 0$ in the optical band. Motivated by these considerations, we characterize the frequency and structural properties of bars at $z \sim 0$ in the optical and NIR bands, by ellipse-fitting the B and H images of 180 spirals in the OSUBSGS (Eskridge et al. 2002), and applying quantitative criteria in order to identify and characterize bars. We determine the inclination of the outer disk and exclude highly inclined ($i > 60^\circ$) galaxies to derive a sample S4 of 136 moderately inclined spirals. For this sample, we derive bar properties both before and after deprojection to face-on. Our study complements existing work on OSUBSGS based on Fourier amplitudes (Block et al. 2002; Buta et al. 2005) and visual classification (Eskridge et al. 2000), and it can be compared with studies (Jogee et al. 2004; Elmegreen et al. 2004; Zheng et al. 2005) of intermediate redshift ($z \sim 0.2$ – 1.0) bars employing the same ellipse-fitting methodology. Our results are summarized below.

(1) The optical and NIR bar fraction at $z \sim 0$: For our sample, which is dominated by galaxies with $M_V \sim -20$ to -22 , we find a deprojected bar fraction at $z \sim 0$ of $f_{\text{NIR1}} \sim 60\% \pm 6\%$ in the near-infrared H band, and $f_{\text{optical1}} \sim 44\% \pm 6\%$ in the optical B -band images. The latter likely miss bars obscured by dust and star formation. Deprojection does not make any significant changes to the global B - and H - band bar fractions, which are 45% and 58% before deprojection, and change by only a factor of 0.97 and 1.03, respectively, after deprojection. This is encouraging for large studies of bars at intermediate redshift (e.g., Jogee et al. 2004, Elmegreen et al. 2004, Zheng et al. 2005), where deprojection is not performed.

(2) Comparison of optical properties of bars at $z \sim 0$ and at intermediate redshifts: Studies of bars at $z \sim 0.2$ – 1.0 (lookback times of 3–8 Gyr) based on HST ACS observations in the Tadpole field, the GEMS and GOODS fields, and COSMOS surveys trace bars in the *rest-frame optical*. R/I to V/B bands (7586 Å to 4550 Å). Therefore, in order to avoid the pernicious effects of bandpass shifting, it is essential that ACS studies of bars at $z \sim 0.2$ – 1.0 compare their rest-frame optical results to the optical bar fraction at $z \sim 0$, rather than to the significantly higher NIR bar fraction at $z \sim 0$.

Furthermore, at $z \sim 0.2$ – 1.0 , it is essential to apply cut-offs in absolute magnitude, bar size, and bar ellipticity in order to ensure a complete sample, adequate spatial resolution, and reliable bar identification. After applying cutoffs in absolute magnitude ($M_V < -19.3$), bar size ($a_{\text{bar}} \geq 1.5$ kpc), and bar ellipticity ($e_{\text{bar}} \geq 0.4$), Jogee et al. (2004) found a rest-frame optical bar fraction of $f_{\text{optical2}} \sim 30\% \pm 6\%$ at $z \sim 0.2$ – 1.0 . A constant and similar optical bar fraction (23% to 40%) out to $z \sim 1$ is also reported by Elmegreen et al. (2004). In order to derive the equivalent optical bar fraction for comparison at $z \sim 0$, we applied the exact same cutoffs to the OSUBSGS optical data. With a cut off of $M_V < -19.3$, the optical bar fraction $z \sim 0$ drops from 45% (61/136) to 43%. Applying a further cutoff of $a_{\text{bar}} \geq 1.5$ kpc makes it drop to 36%. Finally, a third cutoff of $e_{\text{bar}} \geq 0.4$ reduces optical B -band bar fraction at $z \sim 0$ to $f_{\text{optical3}} \sim 34\% \pm 6\%$. The result that f_{optical2} is comparable to f_{optical3} rules out scenarios where the *optical* bar fraction in *bright* disks declines strongly with redshift. It

allows for models where the optical bar fraction is either constant, or rises with redshift.

(3) Distribution of bar strengths $z \sim 0$ as characterized by ellipse-fitting: In this study, we use the maximum bar ellipticity e_{bar} from ellipse-fits as a partial measure of the bar strength. Only a very small proportion (7% in B ; 10% in H) of bars are very weak as characterized by e_{bar} from ellipse fits ($0.25 \leq e_{\text{bar}} \leq 0.40$), while the majority of bars (70% in B ; 71% in H) have moderate to high ellipticities ($0.50 \leq e_{\text{bar}} \leq 0.75$). We find no evidence for bimodality in the distribution of bar strength, as characterized by e_{bar} in the B or H bands, in agreement with Buta et al. (2005).

(4) Bar fraction and strength, as characterized by ellipse-fitting, as a function of RC3 Hubble type at $z \sim 0$: The deprojected bar fraction is 60% in H and 44% in B , confirming the ubiquity of local bars. In the B band, the bar fraction is lower with respect to the H band by ~ 1.2 – 1.5 for Hubble types S0s to Scs, and by ~ 2.5 for Sds/Sms. This is consistent with the higher obscuration in dusty, gas-rich late types. The bar fraction and bar strength, as characterized by e_{bar} , in the H band shows no systematic variation across Hubble types Sa to Scd.

(5) Comparison with RC3 visual bar classes: Of the 42, 47, and 46 galaxies in our sample that have an RC3 visual bar class of ‘A’ (unbarred), ‘B’ (strongly barred), and ‘AB’ (weakly barred), respectively, our quantitative characterization (§ 3.3) shows that 5%, 85%, and 41% host bars in B -band images and 19%, 87%, and 65% host bars in H -band images. Thus, quantitative characterization of bars differs significantly from RC3 bar classes for the RC3 bar class ‘AB’. Furthermore, the mean bar strength, as characterized by the maximum bar ellipticity e_{bar} , is higher for RC3 visual class ‘B’ than for class ‘AB’, but the two classes have significant overlap in the range $e_{\text{bar}} \sim 0.5$ – 0.7 . Thus, RC3 bar types should be used with caution and may be misleading.

(6) Sizes of bars and disks at $z \sim 0$: The sizes or semi-major axes a_{bar} of large-scale bars in the local Universe lie in the range ~ 1 to 14 kpc, with the majority of bars (68% in B and 76% in H) having $a_{\text{bar}} \leq 5$ kpc. Bar and disk sizes are correlated with an average slope of ~ 0.9 , albeit with a large scatter of several kpc in bar size at a given disk size. The ratio (a_{bar}/R_{25}) lies primarily in the range 0.1 to 0.5, with only a minority of galaxies having larger values out to 0.95. The correlation between bar and disk sizes, and the narrow range in a_{bar}/R_{25} suggests that the growths of the bar and disk may be intimately tied. The fact that (a_{bar}/R_{25}) is generally well below 1.0 suggests that the CR of disk galaxies lies well inside their R_{25} radius, assuming that bars end near the CR.

(7) Constraints on the robustness of bars: Our findings that the majority (60%) of spirals are barred in the infrared and that most ($\sim 71\%$ – 80%) of these bars have primarily moderate to high ellipticities ($0.50 \leq e_{\text{bar}} \leq 0.80$) suggest that DM halos of present-day spirals have at most a mild triaxiality, with a maximum equatorial axis ratio $b/a \sim 0.9$ in the potential. We also found that the bar fraction and mean bar strength (as characterized by the maximum bar ellipticity e_{bar}) are relatively constant across Hubble types Sa to Scd, and there is no bimodality in e_{bar} . Taken together, our results are easily reconciled with scenarios where bars in present-day galaxies are relatively

robust against the range in gas mass fractions, gas inflows, and CMC components present across Hubble types Sa to Scd. Our results do not necessarily rule out models where bars are easily destroyed by bar-driven gas inflows. They do, however, imply that if such an easy destruction occurs, then there must be a very efficient mechanism that not only regenerates bars on a short timescale, but is also very well tuned to the bar destruction rate so that it can reproduce the observed constant optical bar fraction in bright galaxies over the last 8 Gyr.

S.J. and I.M. acknowledge support from NSF grant AST-0607748, NASA LTSA grant NAG5-13063, as well as *HST* grants G0-1048 and G0-10395 from STScI, which is operated by AURA, Inc., for NASA, under NAS5-26555.

The Ohio State University Bright Spiral Galaxy Survey, was funded by grants AST-9217716 and AST-9617006 from the United States National Science Foundation, with additional support from the Ohio State University. We thank Pat Shopbell, Peter Teuben, and Stuart Vogel for their assistance with the Zodiac and MIRIAD packages; Seppo Laine for sharing his deprojection code from Laine et al. (2002); and James Davies for help with IRAF and IGI visualization routines. We also thank Paul Eskridge, Ron Buta, Fabio Barazza, Debbie Elmegreen, Isaac Shlosman, Ingo Berentzen, Seppo Laine, Juntao Shen, Victor Debattista, Lia Athanassoula, Françoise Combes, Frederic Bournaud, Jerry Sellwood, and Johan Knapen for useful discussions.

REFERENCES

- Abraham, R. G., Merrifield, M. R., Ellis, R. S., Tanvir, N. R., & Brinchmann, J. 1999, *MNRAS*, 308, 569
- Abraham, R. G., & Merrifield, M. R. 2000, *AJ*, 120, 2835
- Aguerri, J. A. L., Debattista, V. P., & Corsini, E. M. 2003, *MNRAS*, 338, 465
- Athanassoula, E. 1992a, *MNRAS*, 259, 328
- Athanassoula, E. 1992b, *MNRAS*, 259, 345
- Athanassoula, E. 2002, *ApJL*, 569, 83
- Athanassoula, E. 2003, *MNRAS*, 341, 1179
- Athanassoula, E. 2005, *MNRAS*, 358, 1477
- Athanassoula, E., Lambert, J. C., & Dehnen, W. 2005, *MNRAS*, 363, 496
- Barazza, F. D., Jogee, S., & Marinova, I. 2006, *IAU Symposium*, 235 (astro-ph/0610561)
- Berentzen, I., Shlosman, I., & Jogee, S. 2006, *ApJ*, 637, 582
- Berentzen, I., & Shlosman, I. 2006, *ApJ*, 648, 807
- Block, D. L., Bournaud, F., Combes, F., Puerari, I., & Buta, R. 2002, *A&A*, 394, L35
- Bournaud, F., & Combes, F. 2002, *A&A*, 392, 83
- Bournaud, F., Combes, F., & Semelin, B. 2005, *MNRAS*, 364, L18
- Bureau, M., & Athanassoula, E. 2005, *ApJ*, 626, 159
- Buta, R., Block, D. L., & Knapen, J. H. 2003, *AJ*, 126, 1148
- Buta, R., Laurikainen, E., & Salo, H. 2004, *AJ*, 127, 279
- Buta, R., Vasylyev, S., Salo, H., & Laurikainen, E. 2005, *AJ*, 130, 506
- Combes, F., Debbasch, F., Friedli, D., & Pfnegger, D. 1990, *A&A*, 233, 82
- Curir, A., Mazzei, P., & Murante, G. 2006, *A&A*, 447, 453
- Debattista, V. P., & Sellwood, J. A. 1998, *ApJL*, 493, L5
- Debattista, V. P., & Sellwood, J. A. 2000, *ApJ*, 543, 704
- Debattista, V. P., Corsini, E. M., & Aguerrri, J. A. L. 2002, *MNRAS*, 332, 65
- Debattista, V. P., Mayer, L., Carollo, C. M., Moore, B., Wadsley, J., & Quinn, T. 2006, *ApJ*, 645, 209
- de Vaucouleurs, G., de Vaucouleurs, A., Corwin Jr., H. G., Buta, R. J., Paturel, G., & Fouque, P. 1991, *Third Reference Catalogue of Bright Galaxies* (New York: Springer) (RC3)
- Dubinski, J. 1994, *ApJ*, 431, 617
- Elmegreen, B. G., & Elmegreen, D. M. 1985, *ApJ*, 288, 438
- Elmegreen, B. G. 1994, *ApJL*, 425, L73
- Elmegreen, B. G., Elmegreen, D. M., Chromey, F. R., Hasselbacher, D. A., & Bissell, B. A. 1996, *AJ*, 111, 2233
- Elmegreen, B. G., Elmegreen, D. M., & Hirst, A. C. 2004, *ApJ*, 612, 191
- Erwin, P. 2005, *MNRAS*, 364, 283
- Eskridge, P. B., et al. 2000, *AJ*, 119, 536
- Eskridge, P. B., et al. 2002, *ApJS*, 143, 73
- Friedli, D., Wozniak, H., Rieke, M., Martinet, L., & Bratschi, P. 1996, *A&A Suppl.*, 118, 461
- Giavalisco, M., et al. 2004, *ApJL*, 600, L93
- Hunt, L. K., & Malkan, M. A. 1999, *ApJ*, 516, 660
- Jedrzejewski, R. I. 1987, *MNRAS*, 226, 747
- Jogee, S. 1999, Ph.D. thesis, Yale University
- Jogee, S., Kenney, J. D. P., & Smith, B. J. 1999, *ApJ*, 526, 665
- Jogee, S., Knapen, J. H., Laine, S., Shlosman, I., Scoville, N. Z., & Englmaier, P. 2002a, *ApJL*, 570, L55
- Jogee, S., Shlosman, I., Laine, S., Knapen, J. H., Englmaier, P., Scoville, N. Z., & Wilson, C. D. 2002b, *ApJ*
- Jogee, S., Barazza, F., Rix, H.-W., Shlosman, I. et al. 2004a, *ApJL*, 615, L105
- Jogee, S., Scoville, N., & Kenney, J. D. P. 2005, *ApJ*, 630, 837
- Jogee, S., 2006, *Lecture Notes in Physics*, Vol. 693, "AGN Physics on All Scales", Eds. D. Alloin, R. Johnson, & P. Lira (Springer: Berlin Heidelberg New York), Vol 93, Chapter 6, p 143 (astro-ph/0408383).
- Kazantzidis, S., Kravtsov, A. V., Zentner, A. R., Allgood, B., Nagai, D., & Moore, B. 2004, *ApJL*, 611, L73
- Knapen, J. H., Beckman, J. E., Heller, C. H., Shlosman, I., & De Jong, R. S. 1995, *ApJ*, 454, 623
- Knapen, J. H., Shlosman, I., & Peletier, R. F. 2000, *ApJ*, 529, 93
- Kormendy, J. 1993, in *Proceedings of IAU Symposium 153, Galactic bulges*, ed. H. DeJonghe and H. J. Habing, (Dordrecht: Kluwer), 209
- Kormendy, J., & Kennicutt, R. C. 2004, *ARAA*, 42, 603
- Laine, S., Shlosman, I., Knapen, J. H., & Peletier, R. F. 2002, *ApJ*, 567, 97
- Laurikainen, E., Salo, H., & Rautiainen, P. 2002, *MNRAS*, 331, 880
- Laurikainen, E., Salo, H., & Buta, R. 2004, *ApJ*, 607, 103
- Lisker, T., Debattista, V. P., Ferreras, I., & Erwin, P. 2006, *MNRAS*, 370, 477
- Martin, P. 1995, *AJ*, 109, 2428
- Martinez-Valpuesta, I., Shlosman, I., & Heller, C. 2006, *ApJ*, 637, 214
- Menendez-Delmestre, K. et al., 2004, in "Penetrating Bars Through Masks of Cosmic Dust: The Hubble Tuning Fork Strikes a New Note", Eds. D. Block, I. Puerari, K. Freeman, R. Groess, & E. Block (Springer), pp.787-8
- Menendez-Delmestre, K. et al. 2006, *ApJ*, accepted
- Merrifield, M. R., & Kuijken, K. 1995, *MNRAS*, 274, 933
- Mulchaey, J. S., & Regan, M. W. 1997, *ApJL*, 482, L135
- Pfnegger, D., & Norman, C. 1990, *ApJ*, 363, 391
- O'Neill, J. K., & Dubinski, J. 2003, *MNRAS*, 346, 251
- Rix, H.-W., et al. 2004, *ApJS*, 152, 163
- Regan, M. W., Vogel, S. N., & Teuben, P. J. 1997, *ApJ*, 482, L143
- Scoville, et al. 2006, *ApJS*, submitted (astro-ph/0612306)
- Shen, J., & Sellwood, J. A. 2004, *ApJ*, 604, 614
- Sheth, K., Regan, M. W., Scoville, N. Z., & Strubbe, L. E. 2003, *ApJL*, 592, L13
- Shlosman, I., & Noguchi, M. 1993, *ApJ*, 414, 474
- Tran, H., et al. 2003, *ApJ*, 585, 750
- Tully, R. B. 1988, *Cambridge and New York*, Cambridge University Press, 1988, 221 p., (NBG)
- Weinberg, M. D. 1985, *MNRAS*, 213, 451
- Whyte, L. F., Abraham, R. G., Merrifield, M. R., Eskridge, P. B., Frogel, J. A., & Pogge, R. W. 2002, *MNRAS*, 336, 1281
- Wolf, C., et al. 2004, *A&A*, 421, 913
- Wozniak, H., Friedli, D., Martinet, L., Martin, P., & Bratschi, P. 1995, *A&A Suppl.*, 111, 115
- Zheng, X. Z., Hammer, F., Flores, H., Assémat, F., & Rawat, A. 2005, *A&A*, 435, 507

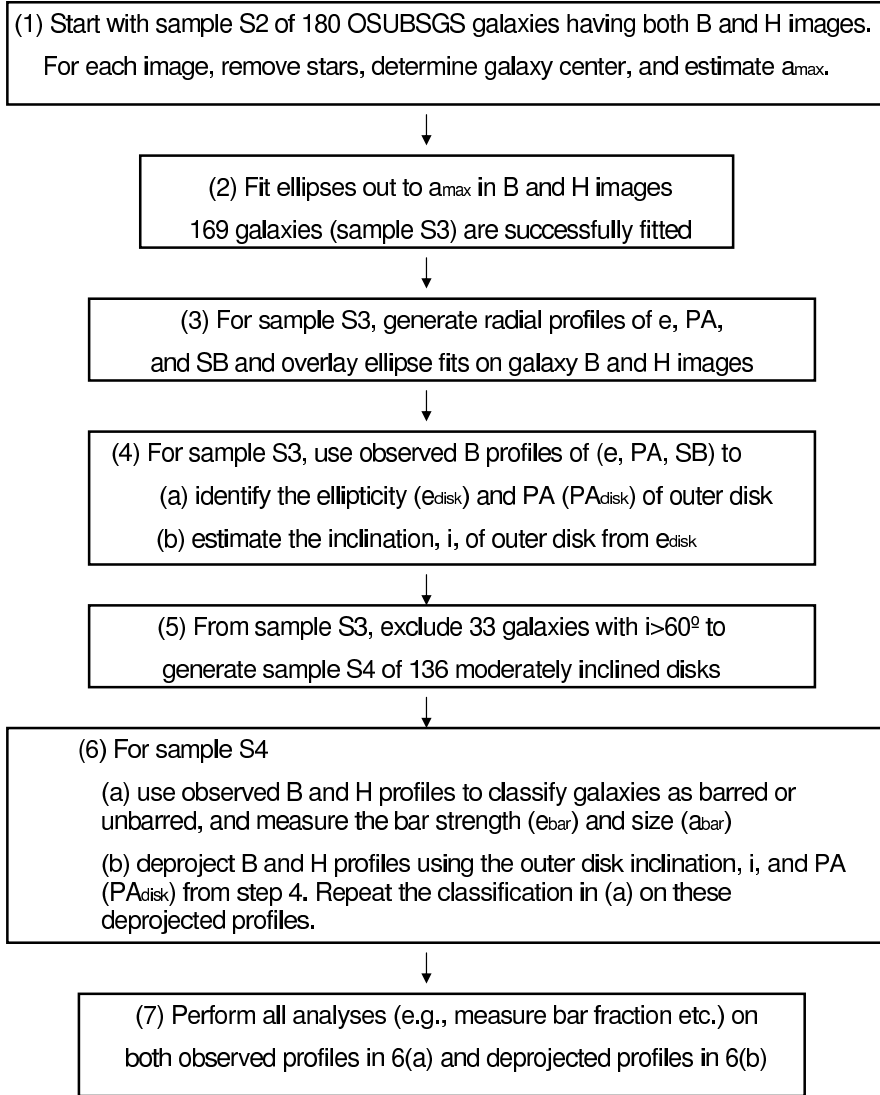


FIG. 1.— **Analysis steps for characterizing bars and disks at $z \sim 0$ from OSUBSGS:** Our procedure of characterizing bars and disks in OSUBSGS galaxies via ellipse fits is schematically illustrated in this figure and described in detail in § 3.1–3.4. For the B and H -band images of the 180 galaxies in sample $S2$, we remove stars, find an accurate center, and determine the maximum semi-major axis of the galaxy, a_{\max} , where the galaxy isophotes reach the sky level. We fit ellipses out to a_{\max} to the B and H images of each galaxy, generate radial profiles of e , PA, and SB, and overlay the ellipses on the galaxy image for inspection. Successful fits are found in both bands for 169 galaxies (sample S3). For sample S3, we use the B -band radial profiles to characterize the inclination i and PA of the outer disk. We exclude 33 galaxies with $i > 60^\circ$ to generate sample S4 of 136 moderately inclined galaxies. For sample S4, we deproject the B and H radial profiles using the outer disk i and PA, and use the deprojected profiles to characterize the properties of barred and unbarred disks. For completeness, we also perform this characterization on the the observed profiles before deprojection.

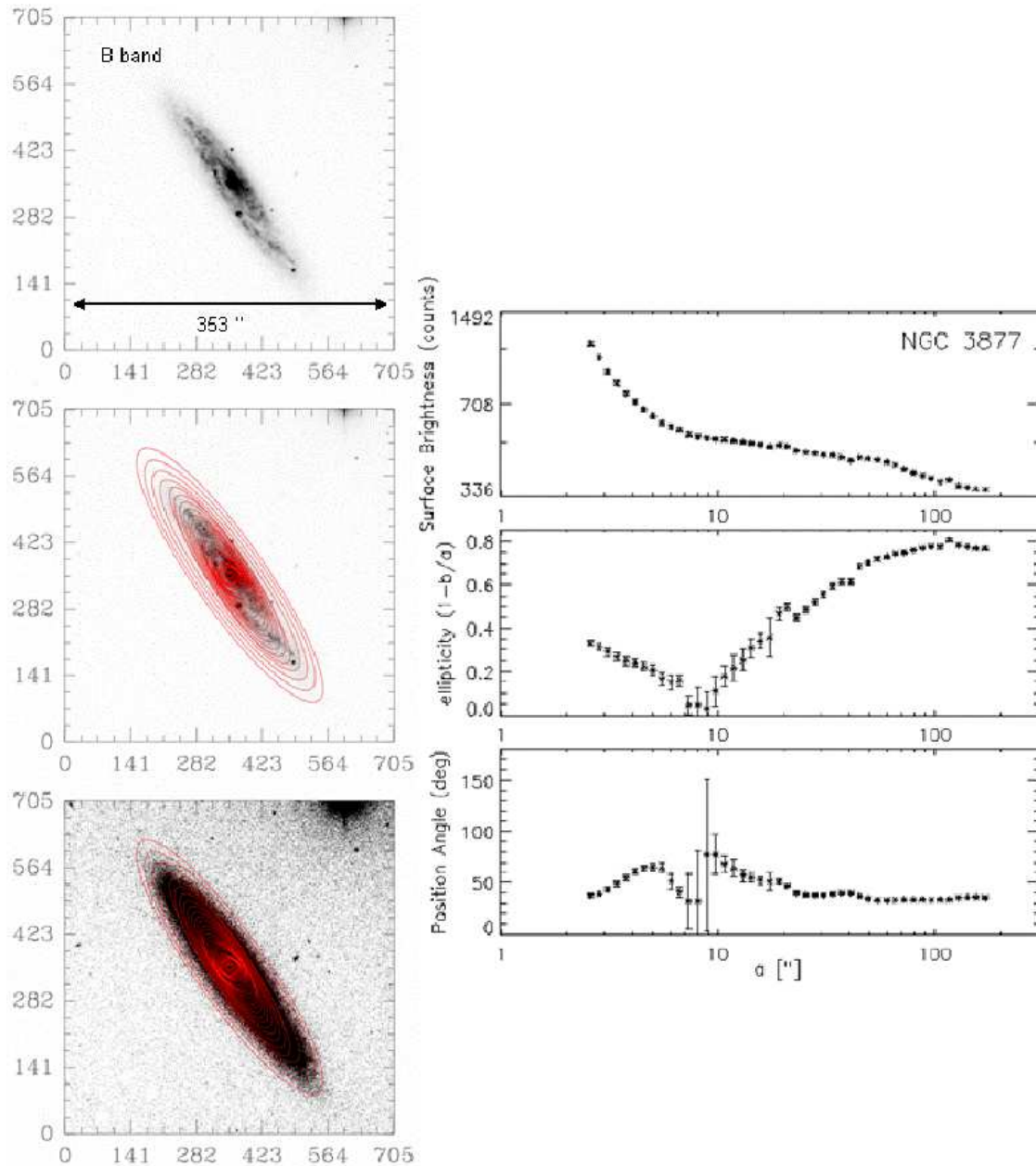


FIG. 2.— **Ellipse fits to the B -band image of an inclined ($i > 60^\circ$) galaxy:** The left panel made of 3 images shows the ellipses fitted to the B -band image of NGC 3877. The top image shows only the galaxy. The scale is shown on the top image in arcseconds, where $1'' = 86$ pc. The middle and bottom images show the ellipses overlaid on the galaxy, with greyscale stretches chosen to emphasize the inner (middle image) and outer (bottom image) regions of the galaxy. Note that ellipses are fitted out to the sky level in the image. The right panel shows the radial profiles of surface brightness (SB), ellipticity (e), and position angle (PA) versus semi-major axis (a) derived from the ellipse fits. The profiles show evidence for some structure in the inner regions, but at $a > 100''$, the e settles to a high value of 0.8, while the PA also settles to a constant value. This is the signature of an inclined disk with $i > 60^\circ$.

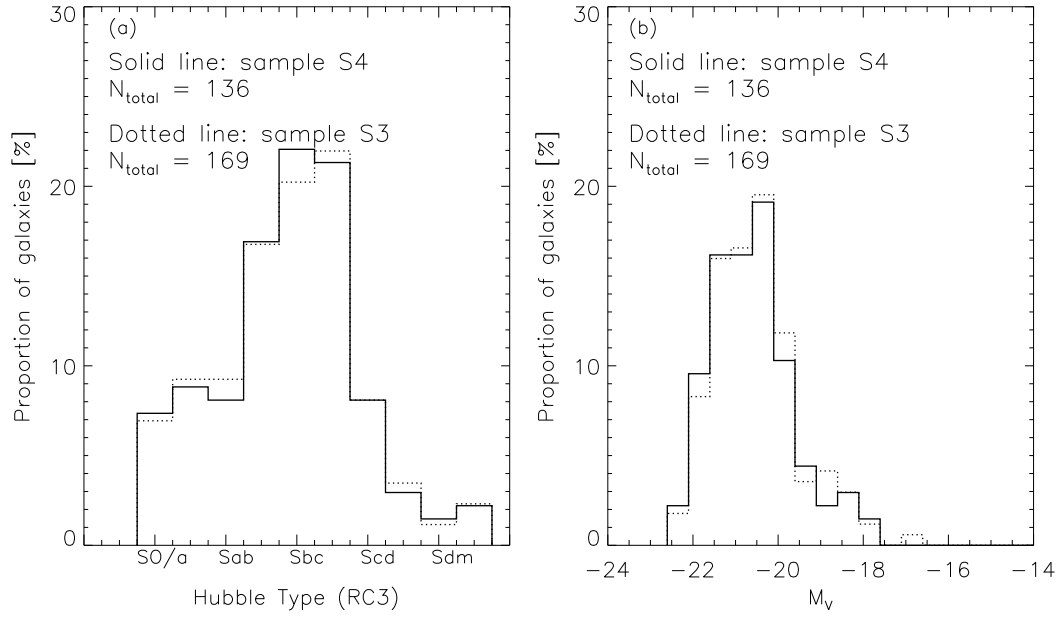


FIG. 3.— **Distribution of Hubble types and absolute magnitudes:** Left: The distributions of RC3 Hubble types are shown for the sample S4 (solid line) of 136 galaxies that include inclined systems, and for the sample S3 (dotted line) produced by excluding 33 galaxies with high inclination ($i > 60^\circ$). This exclusion does not significantly affect the Hubble type distribution of the sample. Right: The distributions of absolute V-band magnitudes for sample S4 (solid line) and S3 (dotted line) are similar as well.

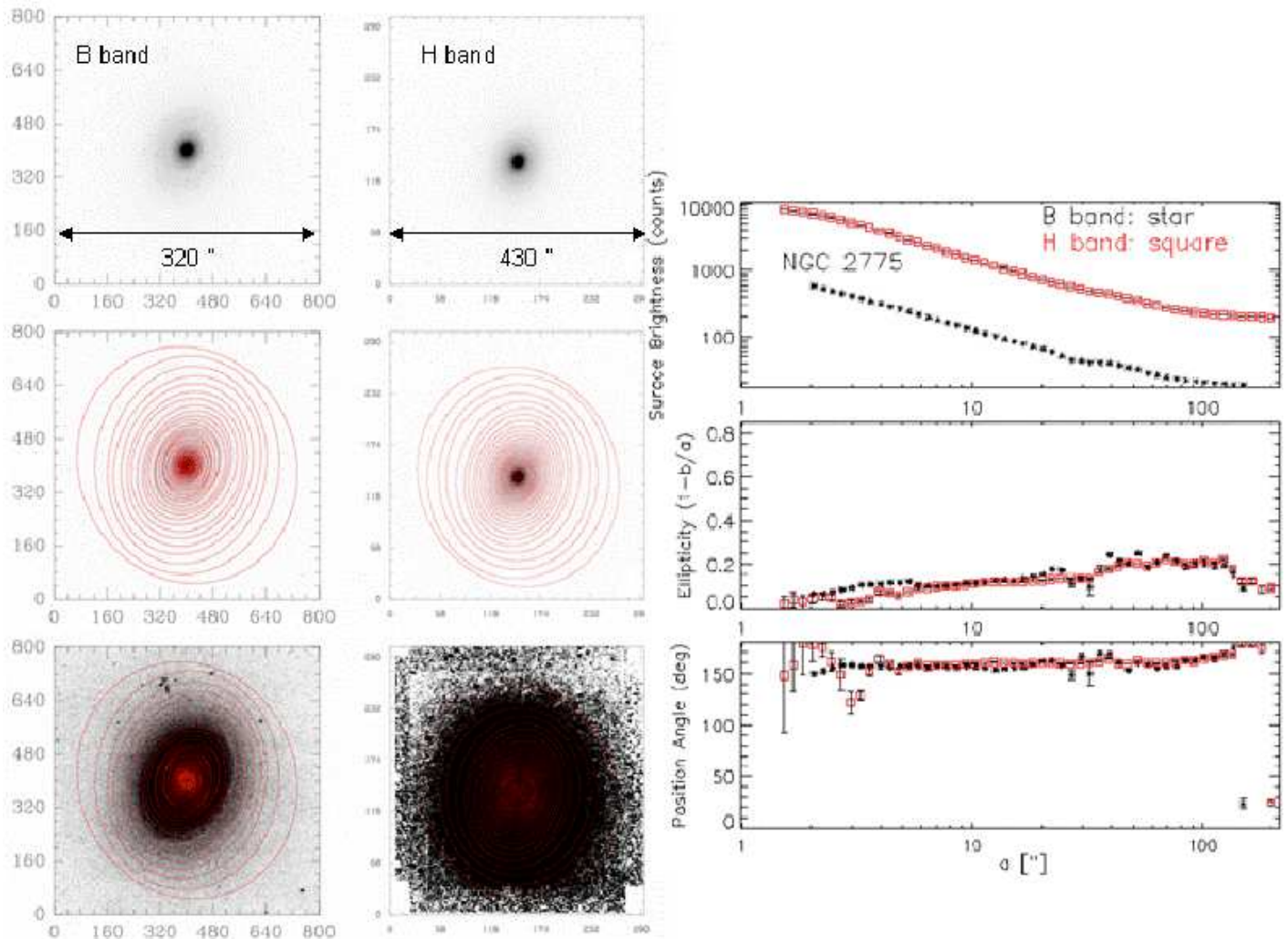


FIG. 4.— **Example of ellipse fits for the unbarred galaxy NGC 2775:** Left and middle panels: They show the ellipse-fits overlaid on the B - and H -band images of the unbarred galaxy NGC 2775. The scales of the B and H images are shown in the top image panels for each band. $1''$ corresponds to 86 pc at the galaxy distance of 17 Mpc. Within each panel, there are 3 images with different greyscale stretches that are chosen to emphasize the inner (middle image) and outer (bottom image) regions of the galaxy. Note that ellipses are fitted out to the sky level in the image. Right panel: This shows the radial profiles of (SB, e , and PA) for the B (stars) and H (squares) bands, derived from the ellipse fits prior to deprojection. The profiles do not show any characteristic bar signatures, such as a smooth rise in e to a maximum above 0.25, concurrent with a PA plateau. The e remains below 0.25 across the galaxy. There is no signature of large-scale structure, such as spiral arms or a bar.

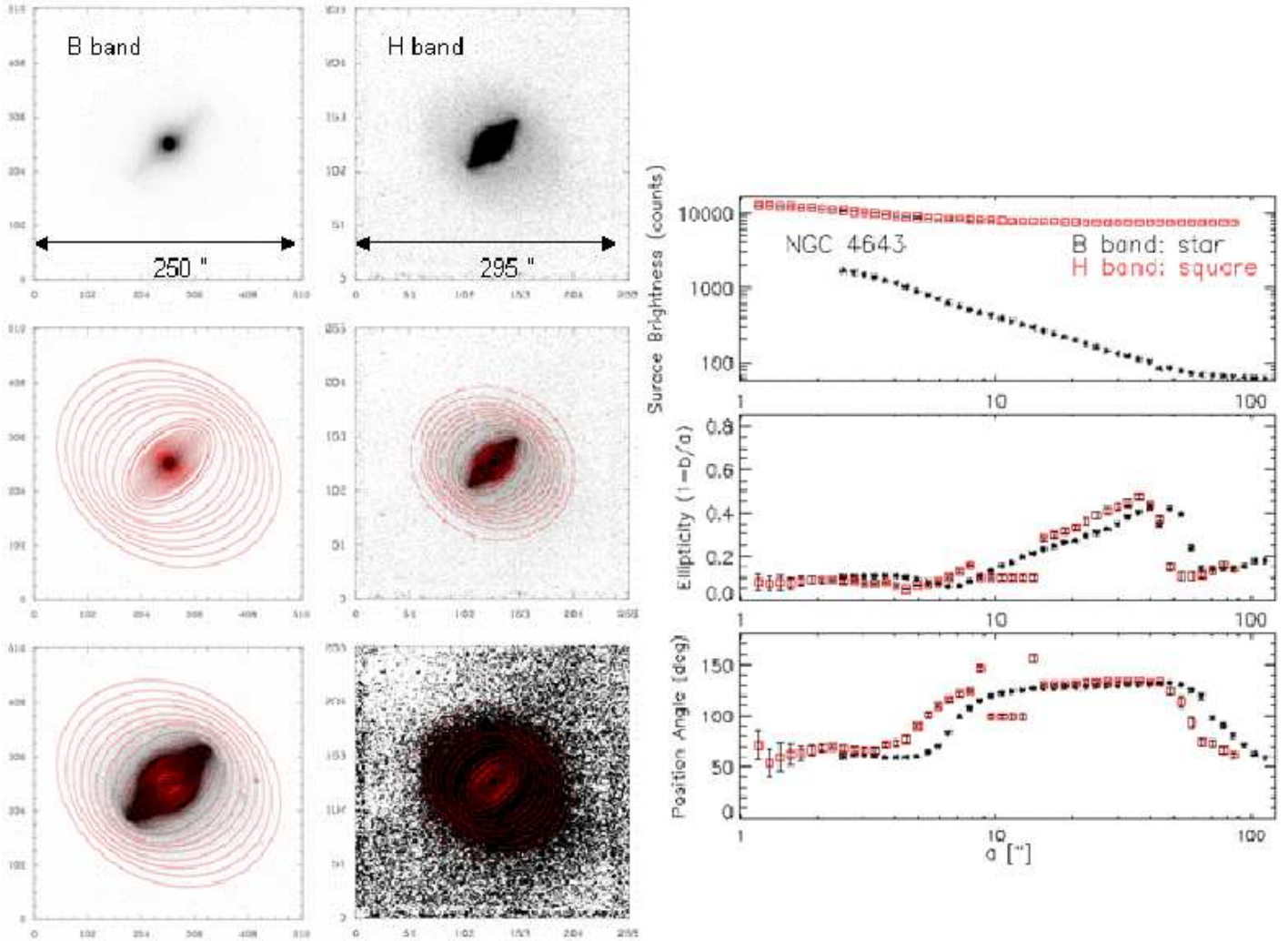


FIG. 5.— **Example of ellipse fits for the barred galaxy NGC 4643:** Left and middle panels: They show the ellipse-fits overlaid on the B - and H -band images of the barred galaxy NGC 4643. The scales of the B and H images are shown in the top image panels for each band. $1''$ corresponds to 130 pc at the galaxy distance of 26 Mpc. Within each panel, there are 3 images with different greyscale stretches that are chosen to emphasize the inner (middle image) and outer (bottom image) regions of the galaxy. Note that ellipses are fitted out to the sky level in the image. Right panel: This shows the radial profiles of (SB, e , and PA) for the B (stars) and H (squares) bands, derived from the ellipse fits and prior to deprojection. The profiles show a clear bar signature. Between $15''$ and $40''$, the e rises smoothly to a global maximum of 0.5, while the PA remains roughly constant. The e then drops to ~ 0.1 , and the PA changes at the transition from the bar to the disk region.

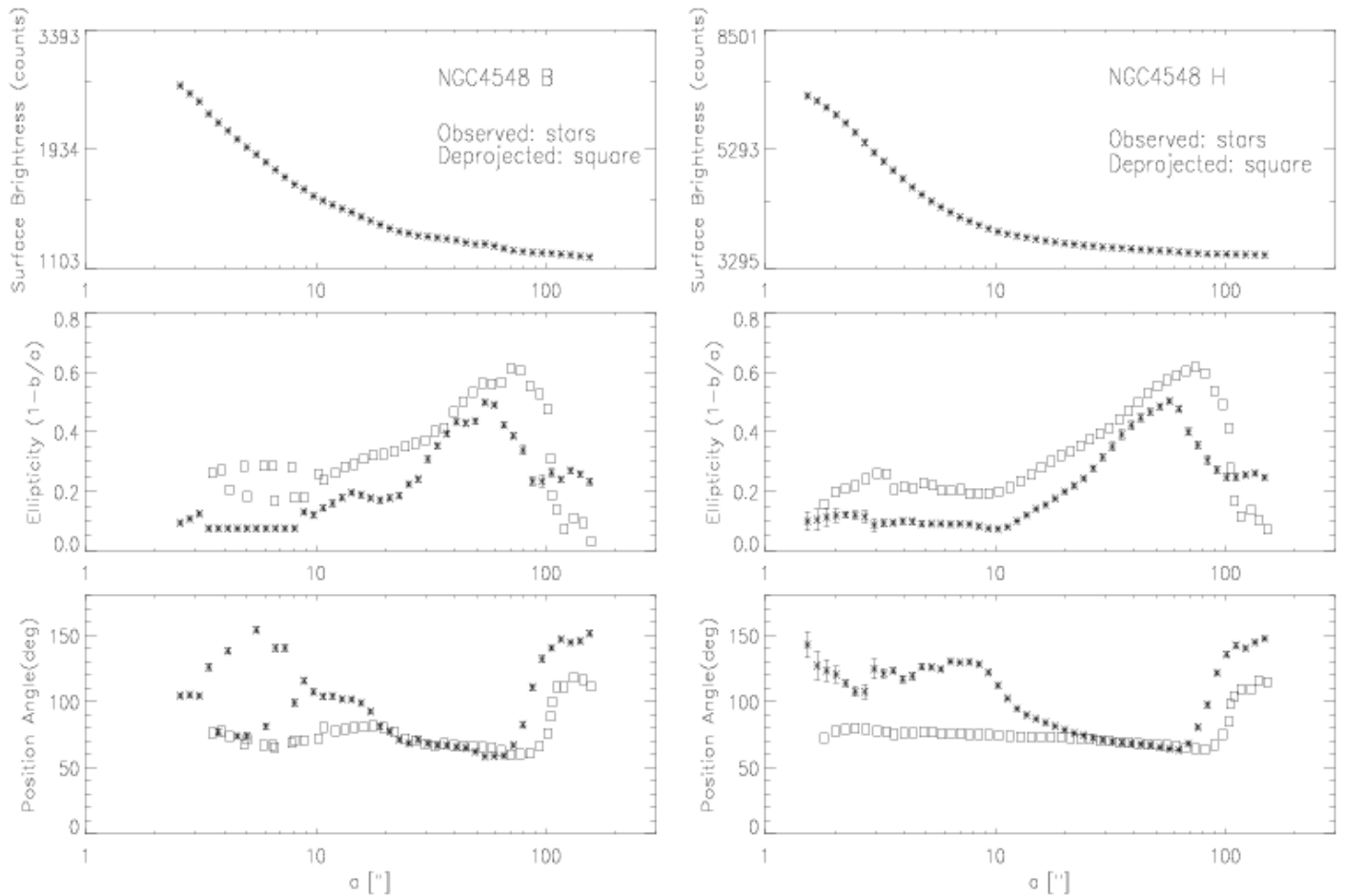


FIG. 6.— **Example of observed and deprojected radial profiles for NGC 4548:** For galaxies in sample S4, we use the inclination i and the PA of the outer disk (from § 3.2) to analytically deproject the observed H - and B -band radial profiles of (e, PA) to face-on. The case for NGC 4548 is illustrated here. The left panel shows the observed (stars) and deprojected (squares) radial profiles in the B band. The right panel shows the observed and deprojected radial profiles in the H band. After deprojection, as expected, the outer disk e is nearly zero in the B band. Note also that the bar size is slightly different and the bar appears somewhat stronger in both bands after deprojection.

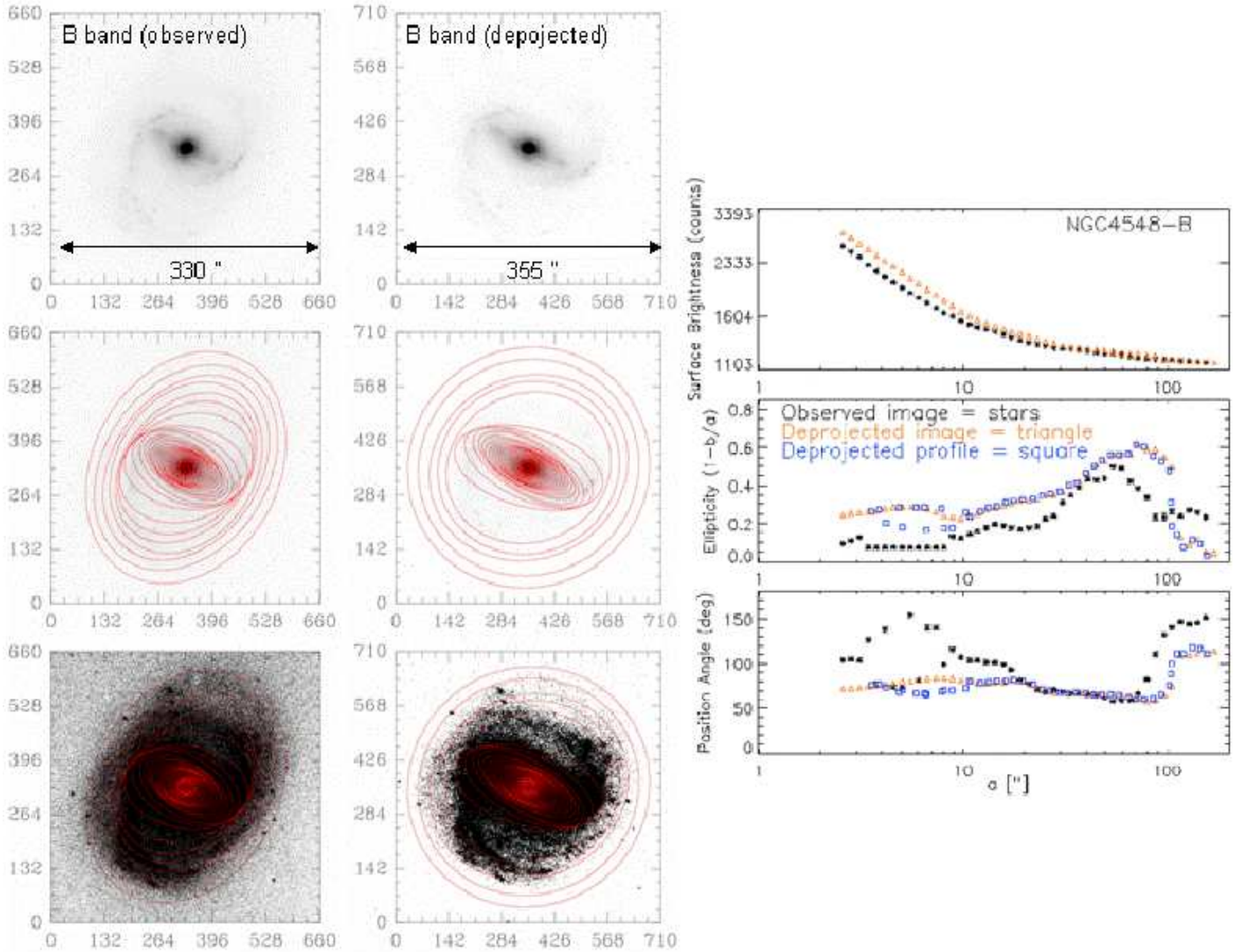


FIG. 7.— **Comparison of the face-on radial profile generated via two different methods:** For the B -band image of NGC 4548, this figure compares the face-on radial profiles of e and PA generated via two different methods. In the first method, ellipses are fitted to the observed image (left panel) to generate the observed radial profile (plotted as stars in the right panel), which is then analytically deprojected to produce the face-on profile (plotted as squares in the right panel). In the second method, the observed image is deprojected with MIRIAD and the resulting deprojected image (middle panel) is fitted with ellipses to generate the second face-on profile (plotted as triangles in the right panel). Note the good agreement between the squares and triangles.

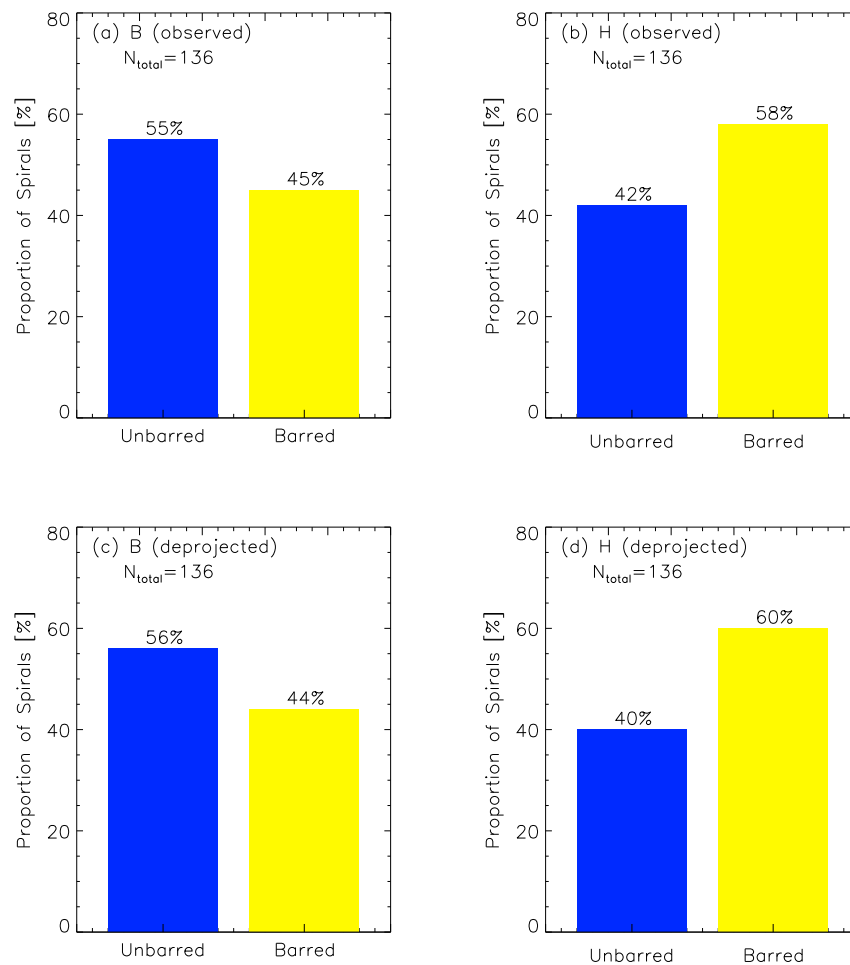


FIG. 8.— **The optical and NIR bar fraction at $z \sim 0$ from OSUBSGS:** We show the fraction of spirals that are barred in the B and H bands, based on ellipse fits of 136 moderately inclined galaxies (sample S4), followed by quantitative characterization of the resulting radial profiles of (e , SB, PA). Top row: The observed bar fraction before deprojection is 45% in the B band (left) and 58% in the H band (right). Bottom row: The deprojected bar fraction is 44% in the B band (left) and 60% in the H band (right).

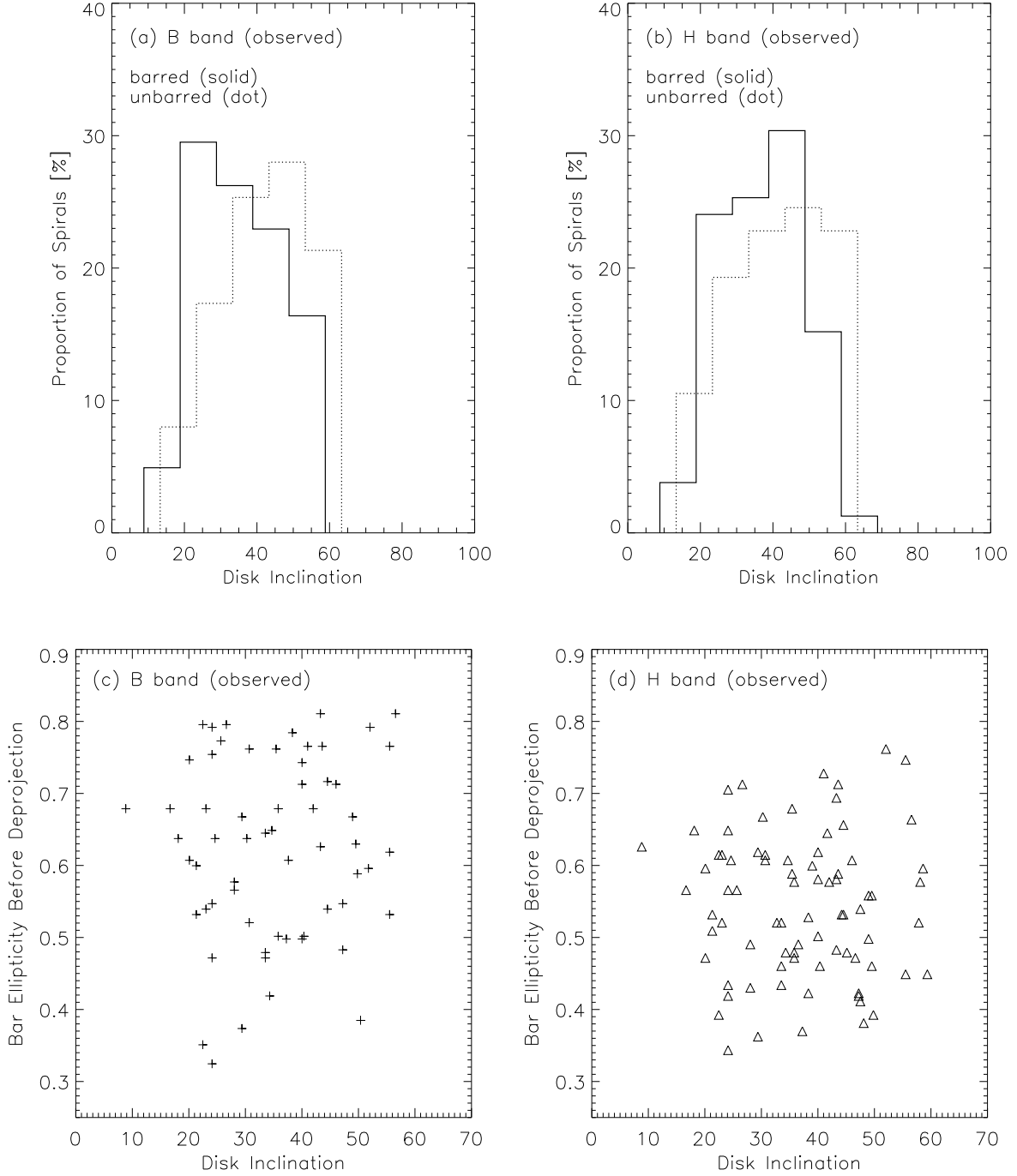


FIG. 9.— **Verifying that bar properties measured prior to deprojection are not biased by galaxy inclination:** Top row: The histograms show the distributions of inclination i for galaxies that were classified as ‘barred’ or ‘unbarred’, prior to deprojection, in the B band (left) and H band (right). Note that there is no correlation with i . Bottom row: The measured bar ellipticity e_{bar} in the B band (left) and H band (right), prior to deprojection, are plotted against the galaxy inclination i . Note that there is no correlation between e_{bar} and i .

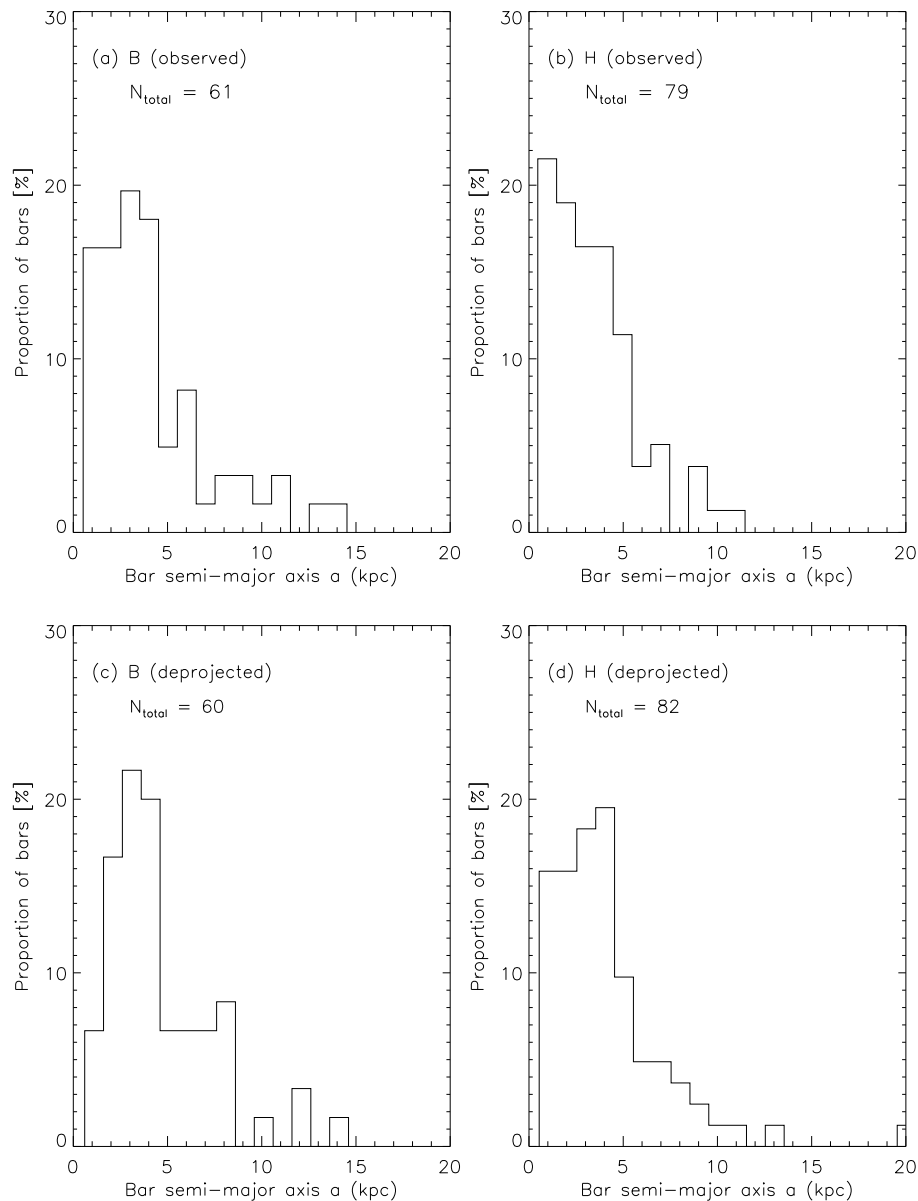


FIG. 10.— **Distribution of bar sizes at $z \sim 0$ from OSUBSGS:** The distributions of bar semi-major axes (a_{bar}) before (top row) and after (bottom row) deprojection are shown, for the *B* (left) and *H* (right) bands. Most (68% in *B* and 76% in *H*) bars have $a_{\text{bar}} \leq 5$ kpc, and $\sim 50\%$ of them cluster in the range 2 to 5 kpc. Deprojection makes several bars appear somewhat larger, but does not otherwise produce a large change in the overall shape of the distributions.

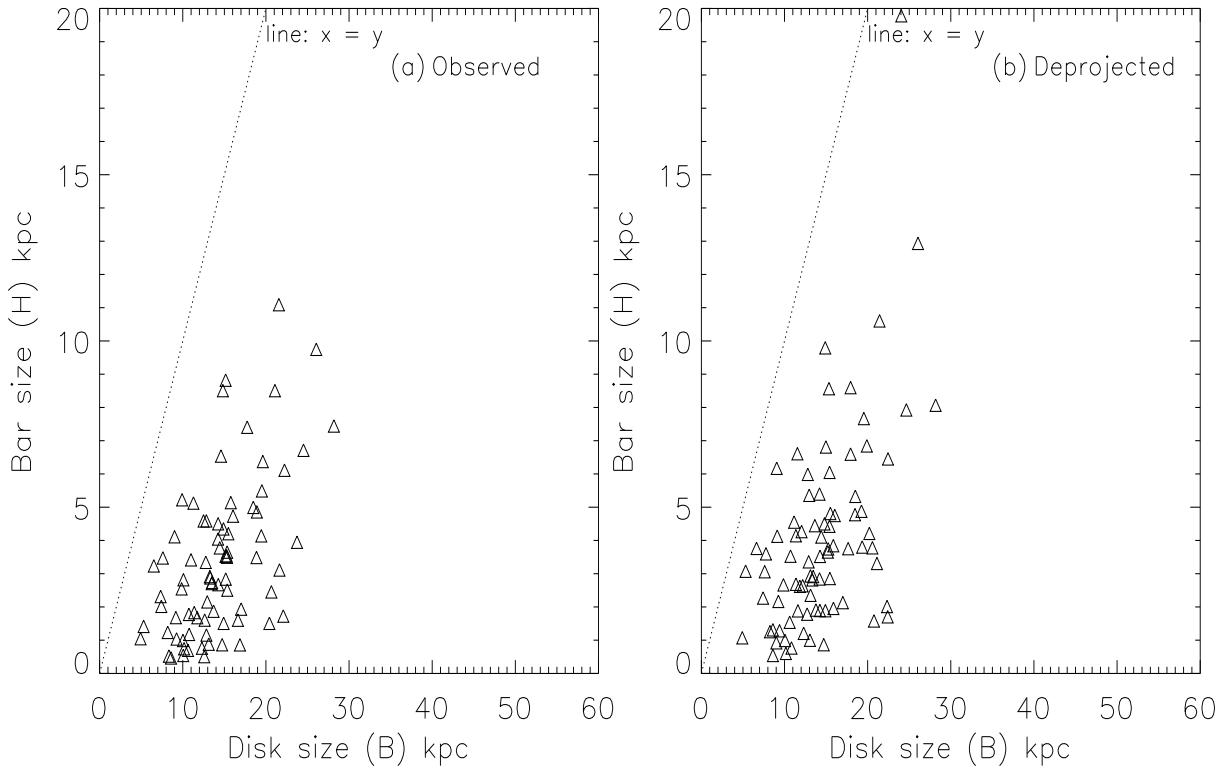


FIG. 11.— **Relationship between H -band bar size and disk size at $z \sim 0$ from OSUBSGS:** The bar semi-major axis in the H band is plotted versus the disk size before (left panel) and after (right panel) deprojection. The disk size is measured in the B -band image which is deeper than the H band and traces the disk further out. The deprojected bar and disk sizes are correlated with an average slope of ~ 0.9 . However, there is a large scatter of several kpc in bar size at a given disk size. For comparison, the dotted line has slope of 1.

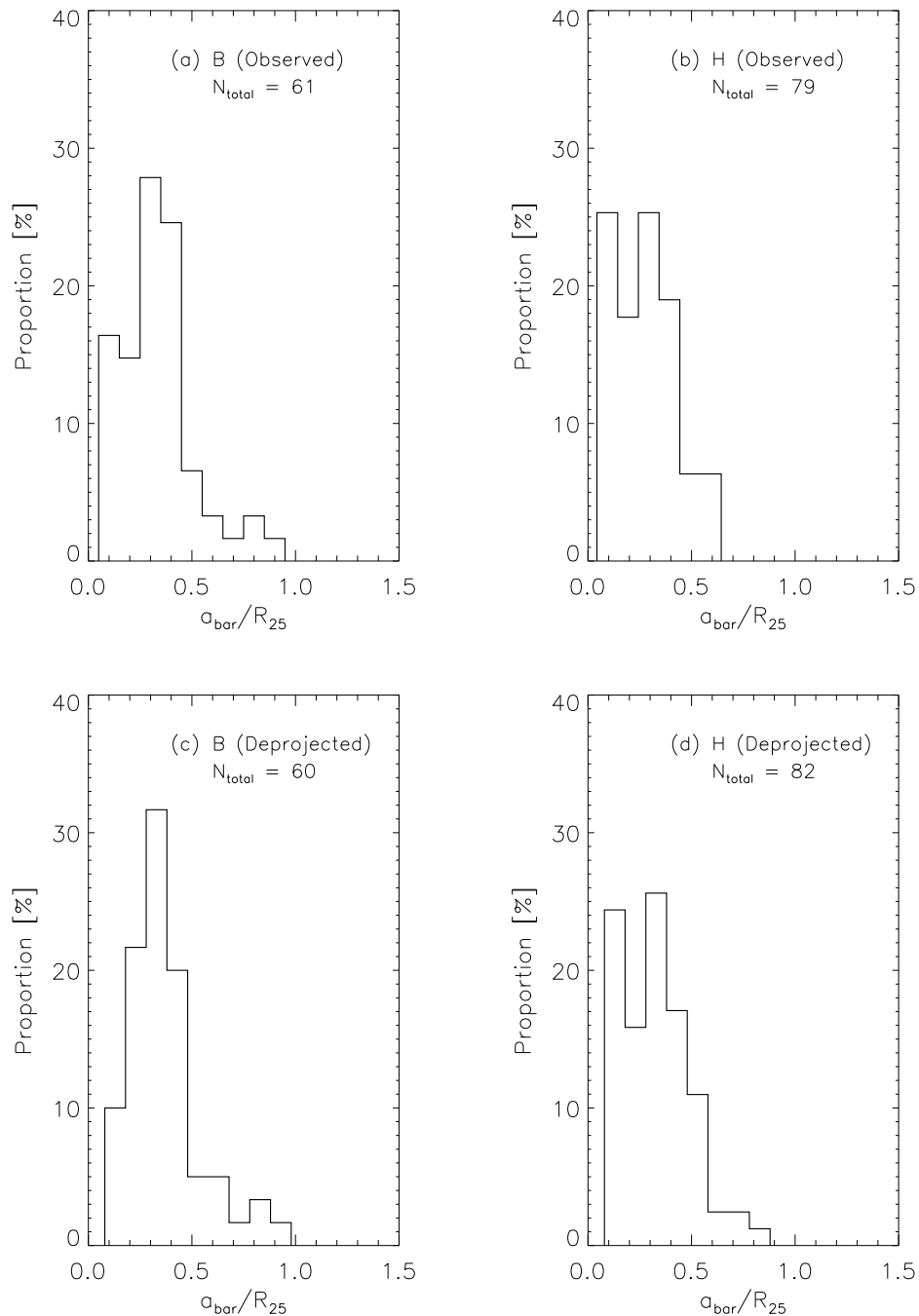


FIG. 12.— **Relationship between bar size and R_{25} at $z \sim 0$ from OSUBSGS:** The ratio of the bar semi-major axis (a_{bar}) to the isophotal radius (R_{25}) where the B -band surface brightness is $25 \text{ mag arcsec}^{-2}$ is shown before (top row) and after (bottom row) deprojection. In the left panels, the bar size (a_{bar}) is determined from the B -band image and in the right panels from the H -band image. We find that the ratio (a_{bar}/R_{25}) is always below 1.0, and lies primarily in the range 0.2 to 0.4 in both H and B bands.

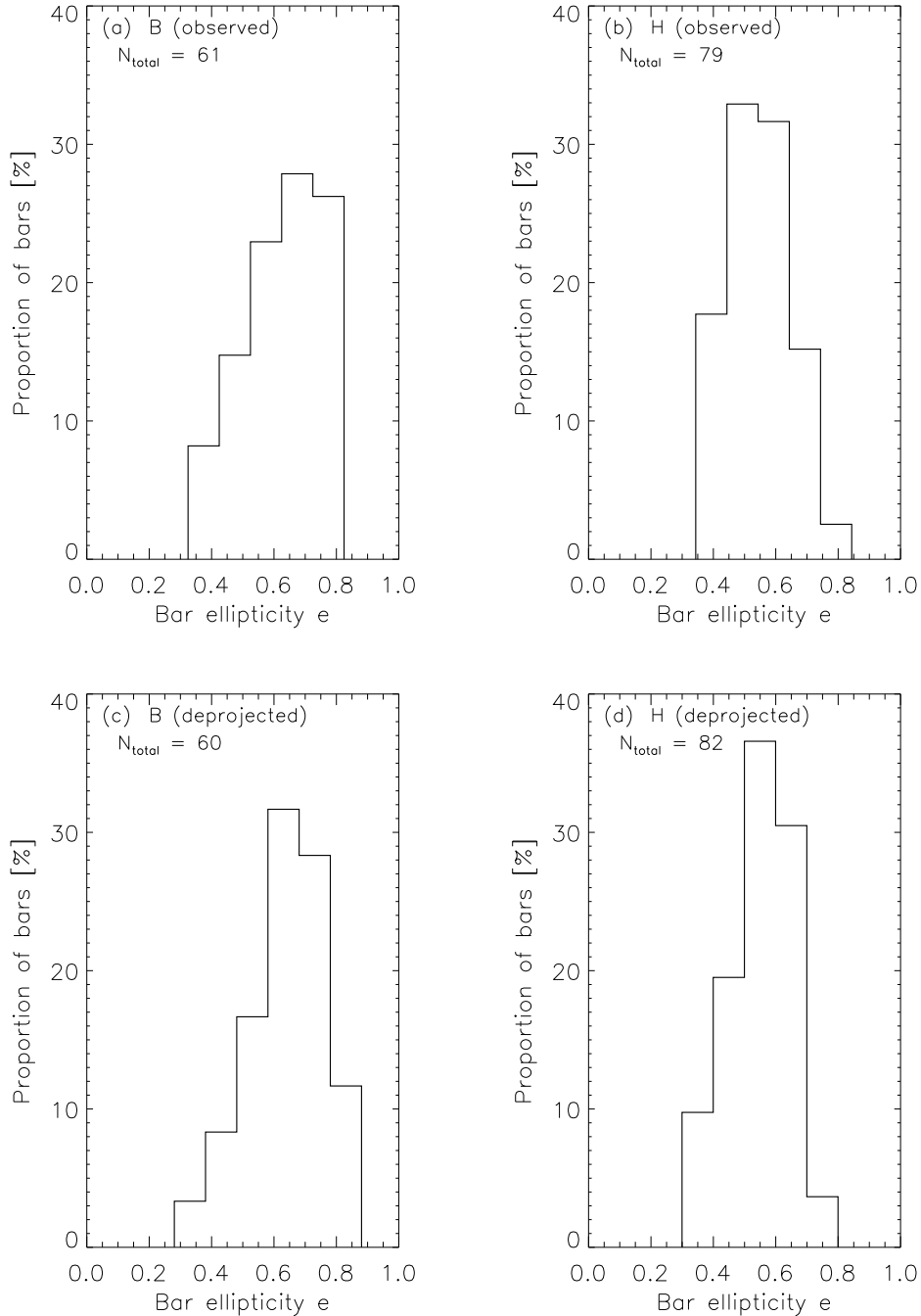


FIG. 13.— **Distributions of bar strengths as characterized by ellipse-fitting at $z \sim 0$ from OSUBSGS:** The distributions of bar strengths (as characterized by e_{bar} from ellipse-fitting) before (top row) and after (bottom row) deprojection, in the B (left) and H (right) bands are shown. It is striking that only a tiny fraction (7% in B ; 10% in H) of bars are very weak with e_{bar} between 0.25–0.40, while the majority of bars (70% in B ; 71% in H) seem to have moderate to high ellipticities, with e_{bar} between 0.50 to 0.75. Furthermore, we find no evidence for bimodality in the distribution of bar strength as characterized by e_{bar} in the B or H bands.

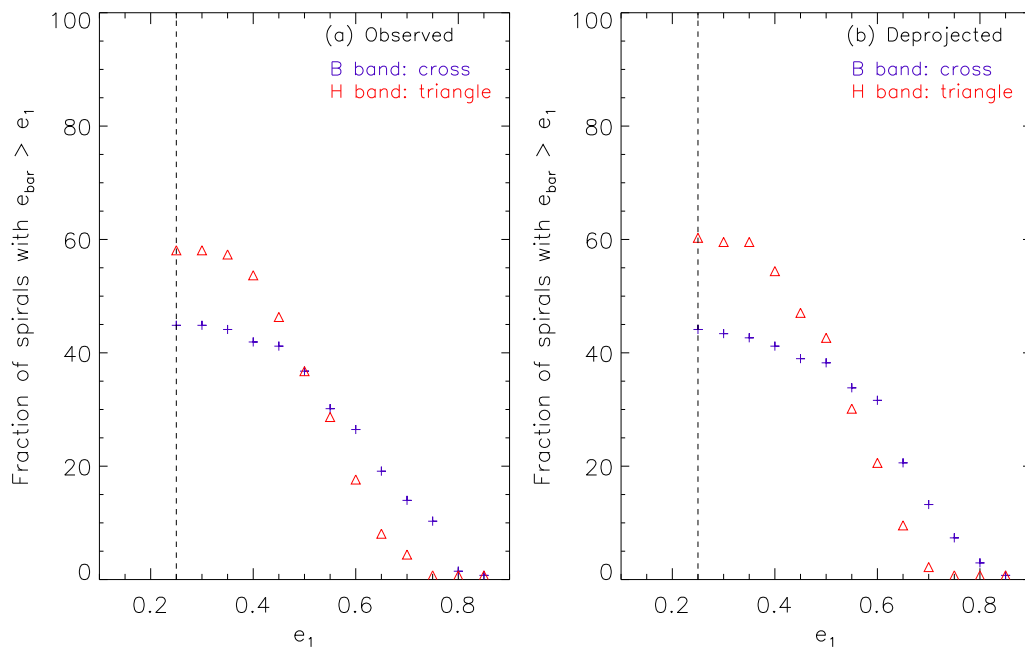


FIG. 14.— **Bar fraction as a function of bar strength as characterized by e_{bar} :** A generalized plot of the fraction of disks with ‘strong’ and ‘weak’ bars is shown before (left panel) and after (right panel) deprojection. The bar strength here is characterized by e_{bar} from ellipse-fitting. The y-axis shows the fraction of spiral galaxies that host bars whose strength e_{bar} exceeds a value e_1 in the B (cross) and H (triangle) bands. Along the the x-axis, e_1 is varied. As e_1 rises from 0.35 to 0.45, 0.55, and 0.75, the deprojected bar fraction in the B band falls from 43% to 39%, 34%, and 7%, respectively, while the bar fraction in the H band falls from 59% to 47%, 30%, and 1%. The flattening of the curve around $e_1 \sim 0.45$ reflects the paucity of very weak (low ellipticity) bars with $0.25 \geq e_{\text{bar}} \leq 0.40$, while the steep fall in the curve for e_1 in the range 0.50–0.75 shows the preponderance of ‘strong’ (high ellipticity) bars.

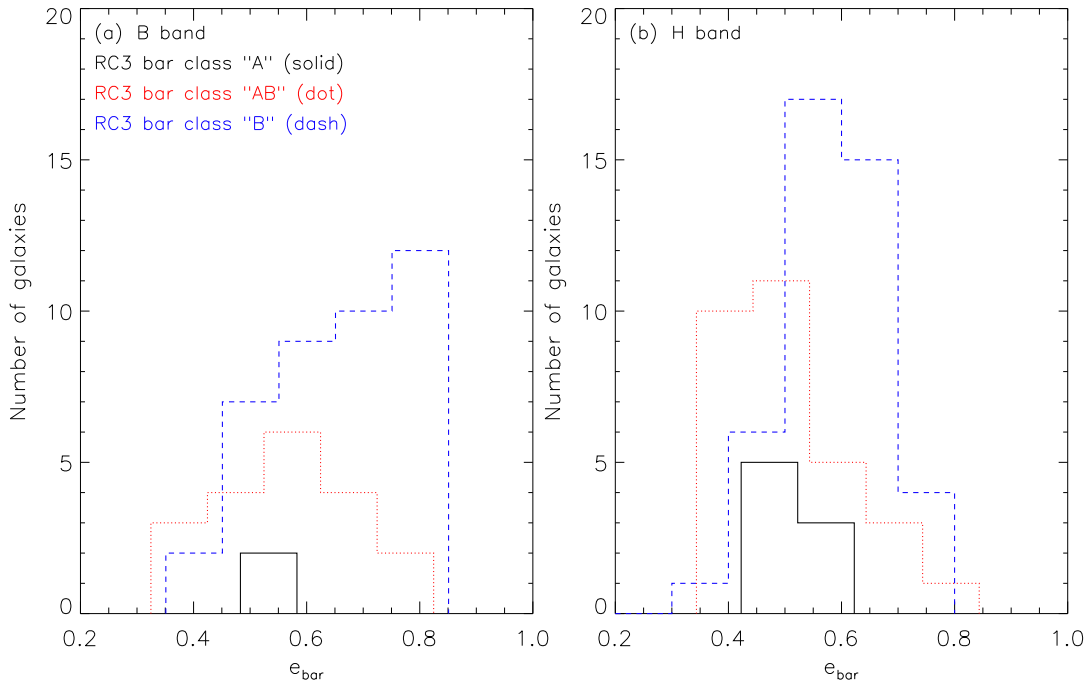


FIG. 15.— **A comparison of RC3 visual bar classes with e_{bar} from ellipse fits:** This figure shows the RC3 visual bar classes for all those galaxies in sample S4 that we classified as barred based on ellipse fits (§ 3.3 and § 3.4). The x-axis shows the bar strength as characterized by e_{bar} from ellipse-fitting in the B (left panel) and H (right panel) bands, prior to deprojection. The three RC3 visual bar classes are based on visual inspection of optical images (de Vaucouleurs et al. 1991) and classes ‘A’ (solid line), ‘AB’ (dotted line), and ‘B’ (dashed line) denote ‘unbarred’, ‘weakly barred’, and ‘strongly barred’ disks, respectively. In the B band, we find that 5%, 41%, and 85%, respectively, of the sample galaxies with RC3 visual classes of ‘A’, ‘AB’, and ‘B’, host bars. In the H band, the corresponding numbers are 19%, 65%, and 87%, respectively. Thus, many galaxies that are classified as unbarred in RC3 turn out to be barred and vice-versa. The mean bar ellipticity e_{bar} is higher for RC3 visual class “B” than for class “AB”, but the two classes have significant overlap in the range $e_{\text{bar}} \sim 0.5\text{--}0.7$.

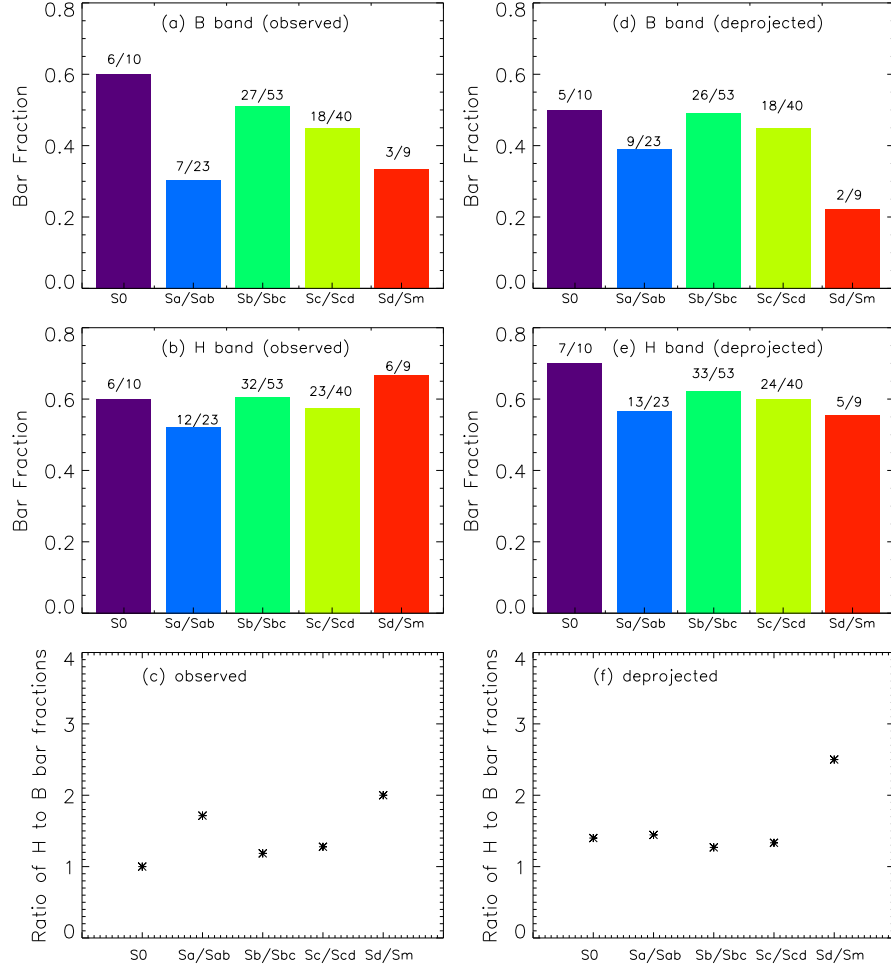


FIG. 16.— **Bar fraction as a function of RC3 Hubble types at $z \sim 0$ from OSUBSGS:** This figure shows what proportion of spirals with different Hubble types host bars. The bar fractions in the B band (top row) and H band (middle row) are shown as a function of RC3 Hubble types, before (left) and after (right) deprojection. The bar fraction above each bin is explicitly given as the ratio (number of barred disks with a given Hubble type/total number of disks of a given Hubble type). The number of galaxies are small for S0 and Sd/Sm types and robust number statistics only apply to RC3 Hubble types Sa to Scd: we find that the H -band bar fraction remains at $\sim 60\%$ across RC2 Hubble types Sa to Scd. The bottom row shows the ratio of the H -band bar fraction to the B -band bar fraction before (left) and after (right) deprojection. In the B band, we find that the bar fraction is lower with respect to the H band by ~ 1.2 – 1.5 for S0s to Scs, and by ~ 2.5 for Sds/Sm. This is likely due to extinction, especially in the dusty, gas-rich late type (Scd–Sm) galaxies.

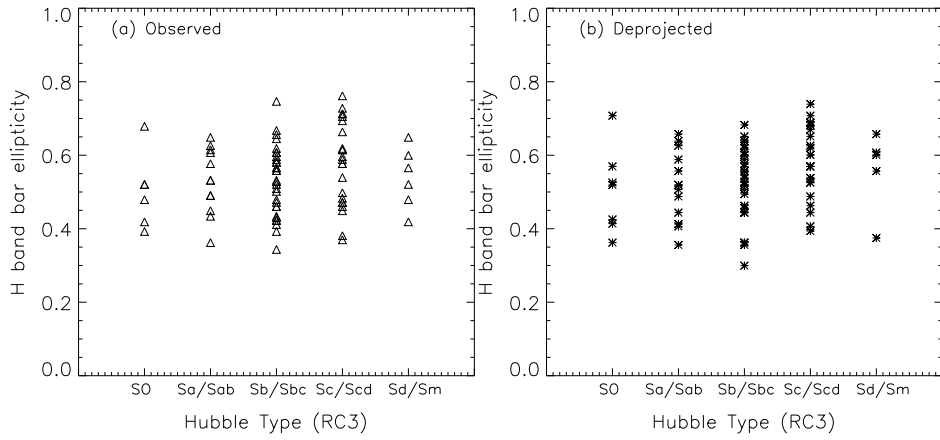


FIG. 17.— **Bar strength as characterized by e_{bar} as a function of RC3 Hubble types at $z \sim 0$ from OSUBSGS:** The bar strength as characterized by the bar ellipticity e_{bar} in the H band is plotted as a function of Hubble types before (left panel) and after (right panel) deprojection. The Hubble types are from RC3 and are binned as in Figure 16. Before deprojection, the number of galaxies in each Hubble type bin is: SO = 6, Sa/Sab = 12, Sb/Sbc = 32, Sc/Scd = 23, Sd/Sm = 6. After deprojection, the corresponding numbers are SO = 7, Sa/Sab = 13, Sb/Sbc = 33, Sc/Scd = 24, Sd/Sm = 5. The number of galaxies are small for S0s and Sd/Sm types and robust number statistics only apply to RC3 Hubble types Sa to Scd. The bar ellipticity e_{bar} lies in the range 0.35–0.80, and shows no systematic variation across Hubble types Sa to Scd, either before or after deprojection.

TABLE 1
GLOBAL PROPERTIES OF SAMPLE S3 (169 GALAXIES) WITH ELLIPSE FITS IN B AND H

Galaxy Name (1)	Hubble Type (RC3) (2)	Bar Type (RC3) (3)	D (Mpc) (4)	D_{25} ($'$) (5)	B_T (mag) (6)	M_V (mag) (7)	L_{IR} ($\log(L_{\odot})$) (8)	L_B ($\log(L_{\odot})$) (9)
Moderately inclined galaxies (N=136)								
IC 0239	SAB(rs)cd	AB	14.2	5.4	11.8	-19.66	-	9.81
IC 4444	SAB(rs)bc	AB	26.9	1.4	12	-20.79	10.53	10.33
IC 5325	SAB(rs)bc	AB	18.1	2.7	11.83	-20.02	-	9.83
NGC 0157	SAB(rs)bc	AB	20.9	3	11	-21.19	10.52	10.53
NGC 0210	SAB(s)b	AB	20.3	4.9	11.6	-20.65	-	10.22
NGC 0278	SAB(rs)b	AB	11.8	2.7	11.47	-19.53	10.03	10.04
NGC 0289	SAB(rs)bc	AB	19.4	8.3	11.72	-20.45	10.03	10.17
NGC 0428	SAB(s)m	AB	14.9	4.6	11.91	-19.4	-	9.85
NGC 0488	SA(r)b	A	29.3	5.4	11.15	-22.05	-	10.74
NGC 0685	SAB(r)c	AB	15.2	3.9	11.95	-19.42	-	9.8
NGC 0864	SAB(rs)c	AB	20	4.4	11.4	-20.66	-	10.27
NGC 1042	SAB(rs)cd	AB	16.7	4.4	11.56	-20.09	-	10.16
NGC 1058	SA(rs)c	A	9.1	3.6	11.82	-18.6	-	9.34
NGC 1073	SB(rs)c	B	15.2	5	11.47	-19.94	-	9.97
NGC 1084	SA(s)c	A	17.1	3.4	11.31	-20.43	10.54	10.3
NGC 1087	SAB(rs)c	AB	19	3.7	11.46	-20.45	10.26	10.28
NGC 1187	SB(r)c	B	16.3	5.4	11.34	-20.28	10.18	10.1
NGC 1241	SB(rs)b	B	26.6	3.6	11.99	-20.98	-	10.12
NGC 1300	SB(rs)bc	B	18.8	6.8	11.11	-20.94	-	10.36
NGC 1302	(R)SB(r)0	B	20	3.8	11.6	-20.8	-	10.24
NGC 1309	SA(s)bc	A	26	2.8	11.97	-20.54	10.24	10.26
NGC 1317	SAB(r)a	AB	16.9	3.1	11.91	-20.12	-	9.87
NGC 1350	(R')SB(r)ab	B	16.9	5	11.16	-20.85	-	10.18
NGC 1371	SAB(rs)a	AB	17.1	6.8	11.57	-20.49	-	10.08
NGC 1385	SB(s)cd	B	17.5	4.6	11.45	-20.28	10.18	10.1
NGC 1493	SB(r)cd	B	11.3	3.9	11.78	-19	-	9.58
NGC 1559	SB(s)cd	B	14.3	3.3	11	-20.13	10.21	10.24
NGC 1617	SB(s)a	B	13.4	4	11.38	-20.2	-	10.08
NGC 1637	SAB(rs)c	AB	8.9	5.1	11.47	-18.92	9.46	9.52
NGC 1703	SB(r)b	B	17.4	3.5	11.9	-19.86	-	-
NGC 1792	SA(rs)bc	A	13.6	6.1	10.87	-20.48	10.33	10.24
NGC 1832	SB(r)bc	B	23.5	2.6	11.96	-20.53	10.28	10.26
NGC 2139	SAB(rs)cd	AB	22.4	2.9	11.99	-20.12	10.16	10.16
NGC 2196	(R')SA(s)a	A	28.8	2.9	11.82	-21.29	-	10.46
NGC 2566	(R')SB(rs)ab pec	B	21.1	4.3	11.83	-20.6	10.6	-
NGC 2775	SA(r)ab	A	17	4.6	11.03	-21.02	-	10.24
NGC 2964	SAB(r)bc	AB	21.9	3	11.99	-20.39	10.36	10.15
NGC 3166	SAB(rs)0	AB	22	3.2	11.32	-21.32	9.94	10.28
NGC 3169	SA(s)a pec	A	19.7	5	11.08	-21.24	10.18	10.37
NGC 3223	SA(s)b	A	38.1	3.6	11.79	-21.93	-	10.88
NGC 3227	SAB(s)a pec	AB	20.6	5.9	11.1	-21.29	10.13	10.26
NGC 3261	SB(rs)b	B	33.4	3.9	12	-	-	10.64
NGC 3275	SB(r)ab	B	42.4	2.8	11.8	-	-	10.61
NGC 3423	SA(s)cd	A	10.9	4	11.59	-19.05	-	9.66
NGC 3504	(R)SAB(s)ab	AB	26.5	2.6	11.82	-20.99	10.72	10.34
NGC 3507	SB(s)b	B	19.8	3.2	11.73	-	-	10.23
NGC 3513	SB(rs)c	B	17	3.2	11.93	-19.65	-	9.98
NGC 3583	SB(s)b	B	34	2.6	11.9	-	10.54	10.61
NGC 3593	SA(s)0	A	5.5	4.8	11.86	-17.78	9.22	9
NGC 3596	SAB(rs)c	AB	23	4.1	11.95	-	-	10.32
NGC 3646	Ring	-	55.8	3.9	11.78	-22.6	-	-
NGC 3681	SAB(r)bc	AB	24.2	2.9	11.9	-20.73	-	10.06
NGC 3684	SA(rs)bc	A	23.4	2.9	12	-20.47	-	10.07
NGC 3686	SB(s)bc	B	23.5	2.9	11.89	-20.54	-	10.17
NGC 3726	SAB(r)c	AB	17	5.5	10.91	-20.73	9.78	10.33
NGC 3810	SA(rs)c	A	16.9	3.8	11.35	-20.37	10.12	10.24
NGC 3885	SA(s)0	A	27.8	2.9	11.89	-21.28	10.27	10.29
NGC 3887	SB(r)bc	B	19.3	3.4	11.41	-	9.8	10.16
NGC 3893	SAB(rs)c	AB	17	4.3	11.16	-	10.2	10.3
NGC 3938	SA(s)c	A	17	4.9	10.9	-20.77	9.93	10.3
NGC 3949	SA(s)bc	AB	17	2.8	11.54	-20.06	9.87	10.16
NGC 4027	SB(s)dm	B	25.6	3.3	11.66	-20.92	10.36	10.41
NGC 4030	SA(s)bc	A	25.9	4	11.42	-	10.64	10.3
NGC 4051	SAB(rs)bc	AB	17	5.4	10.83	-20.97	9.9	10.29
NGC 4123	SB(r)c	B	16.5	4.6	11.98	-19.71	9.76	10.29
NGC 4136	SAB(r)c	AB	9.7	4	11.69	-	-	9.48
NGC 4145	SAB(rs)d	AB	20.7	5.9	11.78	-20.31	-	10.28
NGC 4151	(R')SAB(rs)ab	AB	20.3	6.3	11.5	-20.77	10.2	10.38
NGC 4212	SAc	A	16.8	2.3	11.83	-19.97	9.82	10.02
NGC 4242	SAB(s)dm	AB	7.5	5.2	11.37	-18.55	-	9.36
NGC 4254	SA(s)c	A	16.8	5	10.44	-	10.54	10.53
NGC 4303	SAB(rs)bc	AB	15.2	5.9	10.18	-21.26	10.51	10.48
NGC 4314	SB(rs)a	B	9.7	4.2	11.43	-19.35	-	9.65
NGC 4394	(R)SB(r)b	B	16.8	3.4	11.73	-20.25	-	9.99
NGC 4414	SA(rs)c	A	9.7	4.5	10.96	-19.81	10.56	9.84

TABLE 1—*Continued*

Galaxy Name (1)	Hubble Type (RC3) (2)	Bar Type (RC3) (3)	D (Mpc) (4)	D_{25} ($'$) (5)	B_T (mag) (6)	M_V (mag) (7)	L_{IR} ($\log(L_\odot)$) (8)	L_B ($\log(L_\odot)$) (9)
NGC 4450	SA(s)ab	A	16.8	5	10.9	-21.05	-	10.34
NGC 4457	(R)SAB(s)0	AB	17.4	3.2	11.76	-20.29	-	10.01
NGC 4487	SAB(rs)cd	AB	19.9	3.9	11.63	-	-	10.27
NGC 4496	SB(rs)m	B	13.1	3.7	11.94	-19.17	-	9.8
NGC 4504	SA(s)bc	A	19.5	3.3	11.89	-	-	10.17
NGC 4548	SB(rs)b	B	16.8	5	10.96	-20.98	-	10.3
NGC 4571	SA(r)d	A	16.8	3.6	11.82	-19.82	-	9.94
NGC 4579	SAB(rs)b	AB	16.8	5.4	10.48	-21.47	9.87	10.46
NGC 4580	SAB(rs)a pec	AB	25.6	2.5	11.83	-	-	9.97
NGC 4593	(R)SB(rs)b	B	39.5	3.3	11.67	-	-	10.82
NGC 4618	SB(rs)m	B	7.3	3.1	11.22	-18.54	-	9.44
NGC 4643	SB(rs)0	B	25.7	2.9	11.72	-21.29	-	10.39
NGC 4647	SAB(rs)c	AB	16.8	2.8	11.94	-19.84	9.81	9.93
NGC 4651	SA(rs)c	A	16.8	3.6	11.39	-20.31	9.72	10.22
NGC 4665	SB(s)0	B	17.9	4.2	10.5	-	-	9.94
NGC 4689	SA(rs)bc	A	16.8	3.7	11.6	-20.18	-	10.04
NGC 4691	(R)SB(s)0 pec	B	22.5	3.5	11.66	-20.68	10.32	10.24
NGC 4698	SA(s)ab	A	16.8	3.3	11.46	-20.58	-	10.22
NGC 4699	SAB(rs)b	AB	25.7	3.1	10.41	-22.53	10.12	10.89
NGC 4775	SA(s)d	A	26.6	2.3	11.67	-	-	10.32
NGC 4900	SB(rs)c	B	17.3	2.5	11.9	-19.82	9.73	9.83
NGC 4902	SB(r)b	B	39.2	2.6	11.61	-22.05	-	10.65
NGC 4930	SB(rs)b	B	35	5.4	12	-21.62	-	-
NGC 4939	SA(s)bc	A	44.3	5.6	11.9	-21.97	-	11.16
NGC 4941	(R)SAB(r)ab	AB	6.4	4.2	11.9	-17.97	-	9.12
NGC 4995	SAB(rs)b	AB	28	2.3	12	-21.11	-	10.4
NGC 5005	SAB(rs)bc	AB	21.3	5.6	10.61	-21.83	10.46	10.7
NGC 5054	SA(s)bc	A	27.3	4.6	11.67	-21.27	10.46	10.66
NGC 5085	SA(s)c	A	28.9	3.9	11.96	-	-	10.48
NGC 5101	(R)SB(rs)0	B	27.4	5.4	11.63	-21.54	-	10.57
NGC 5121	(R')SA(s)a	A	22.1	2.2	11.51	-21.16	-	10.08
NGC 5247	SA(s)bc	A	22.2	4.6	10.5	-21.77	10.32	10.57
NGC 5334	SB(rs)c	B	24.7	4.2	11.99	-	-	10.06
NGC 5371	SAB(rs)bc	AB	37.8	4.2	11.32	-22.27	10.67	10.82
NGC 5427	SA(s)c pec	A	38.1	2.3	11.93	-21.54	10.8	10.57
NGC 5483	SA(s)c	A	24.7	4.6	11.93	-	10.05	10.3
NGC 5676	SA(rs)bc	A	34.5	4	11.87	-21.5	10.63	10.77
NGC 5701	(R)SB(rs)0	B	26.1	4.2	11.76	-21.2	-	10.33
NGC 5713	SAB(rs)bc pec	AB	30.4	3.1	11.84	-21.21	10.72	10.43
NGC 5850	SB(r)b	B	28.5	4.6	11.54	-21.52	-	10.47
NGC 5921	SB(r)bc	B	25.2	4.9	11.49	-21.18	-	10.46
NGC 5962	SA(r)c	A	31.8	2.8	11.98	-21.17	10.55	10.46
NGC 6215	SA(s)c	A	20.5	1.9	12	-20.1	10.54	10.53
NGC 6300	SB(rs)b	B	14.3	5.2	10.98	-20.58	10.09	10.32
NGC 6384	SAB(r)bc	AB	26.6	6.3	11.14	-21.7	-	10.72
NGC 6753	(R)SA(r)b	A	40.9	2.5	11.97	-21.92	10.89	-
NGC 6782	(R)SAB(r)a	AB	50.8	2.2	11.84	-	-	-
NGC 6902	SA(r)b	A	35.7	6.8	11.64	-21.83	-	10.33
NGC 6907	SB(s)bc	B	43	3.3	11.9	-21.96	11.03	-
NGC 7083	SA(s)bc	A	38.7	3.2	11.87	-21.72	10.45	10.73
NGC 7205	SA(s)bc	A	20.5	3.2	11.55	-20.61	10.07	10.3
NGC 7213	SA(s)a	A	22	2.1	11.01	-21.59	-	10.34
NGC 7217	(R)SA(r)ab	A	16	3.6	11.02	-20.9	9.9	10.34
NGC 7412	SB(s)b	B	21.1	4.3	11.88	-20.27	-	10.12
NGC 7418	SAB(rs)cd	AB	17.8	3.6	11.65	-	10.01	9.96
NGC 7479	SB(s)c	B	32.4	3.9	11.6	-21.7	10.79	10.64
NGC 7552	(R')SB(s)ab	B	19.5	3.5	11.25	-20.88	11.03	10.25
NGC 7713	SB(r)d	B	8.2	4.6	11.51	-18.38	-	9.58
NGC 7723	SB(r)b	B	23.7	3.9	11.94	-20.66	-	10.31
NGC 7727	SAB(s)a pec	AB	23.3	3.3	11.5	-21.25	-	10.34
NGC 7741	SB(s)cd	B	12.3	4.1	11.84	-19.14	-	9.7

Highly inclined galaxies with $i > 60^\circ$ (N=33)

IC 4402	SA(s)b sp	A	22.9	5	12	-20.24	10.05	-
IC 5052	SbD sp	B	6.7	5	11.16	-18.6	-	9.28
NGC 0625	SB(s)m sp	B	3.9	5	11.91	-16.61	8.57	8.73
NGC 0779	SAB(r)b	AB	17.3	4.4	11.95	-20.03	-	10.2
NGC 0908	SA(s)c	A	17.8	6.1	10.83	-21.07	10.27	10.51
NGC 1003	SA(s)cd	A	10.7	6.3	12	-18.7	-	9.64
NGC 1421	SAB(rs)bc	AB	25.5	3.5	11.95	-20.61	10.25	10.64
NGC 1808	(R)SAB(s)a	AB	10.8	7.6	10.74	-20.24	10.71	10
NGC 1964	SAB(s)b	AB	20	6.1	11.58	-20.7	10.09	10.37
NGC 2090	SA(rs)c	A	10.2	6.8	11.99	-18.84	-	9.61
NGC 2280	SA(s)cd	A	23.2	6.8	10.9	-21.53	10.13	10.6
NGC 3511	SA(s)c	A	15.5	6.8	11.53	-19.99	9.82	10.25
NGC 3675	SA(s)b	A	12.8	5.8	11	-	9.92	10.13
NGC 3705	SAB(r)ab	AB	17	4.6	11.86	-20.08	-	10.25

TABLE 1—*Continued*

Galaxy Name (1)	Hubble Type (RC3) (2)	Bar Type (RC3) (3)	D (Mpc) (4)	D_{25} ($'$) (5)	B_T (mag) (6)	M_V (mag) (7)	L_{IR} ($\log(L_\odot)$) (8)	L_B ($\log(L_\odot)$) (9)
NGC 3877	SA(s)c	A	17	5.1	11.79	-20.16	9.89	10.29
NGC 4062	SA(s)c	A	9.7	4.5	11.9	-18.79	-	9.5
NGC 4100	(P)SA(rs)bc	A	17	5.1	11.89	-19.99	10.04	10.25
NGC 4293	(R)SB(s)0	B	17	6.3	11.26	-20.79	-	10.21
NGC 4388	SA(s)b	A	16.8	5.6	11.76	-20.11	10	10.16
NGC 4448	SB(r)ab	B	9.7	3.8	12	-18.86	-	9.56
NGC 4527	SAB(s)bc	AB	13.5	6.3	11.38	-20.13	10.42	10.08
NGC 4654	SAB(rs)cd	AB	16.8	4.8	11.1	-20.63	10.1	10.32
NGC 4666	SABc	AB	14.1	4.2	11.49	-20.01	10.36	10.1
NGC 4772	SA(s)a	A	16.3	2.8	11.96	-20.02	-	9.7
NGC 4818	SAB(rs)ab pec	AB	21.5	3.4	12	-20.55	9.75	10.46
NGC 4856	SB(s)0	B	21.1	3.8	11.49	-21.12	-	10.3
NGC 5078	SA(s)a sp	A	27.1	4	12	-21.2	10.5	-
NGC 5161	SA(s)c	A	33.5	6.1	12	-21.42	-	10.64
NGC 5448	(R)SAB(r)a	AB	32.6	4	11.93	-	-	10.47
NGC 7184	SB(r)c	B	34.1	6.1	11.65	-21.81	-	10.73
NGC 7582	(R')SB(s)ab	B	17.6	4.5	11.37	-20.61	10.87	10.26
NGC 7606	SA(s)b	A	28.9	5.2	11.51	-21.55	-	10.7
NGC 7814	SA(s)ab: sp	AB	16	5.5	11.56	-20.45	-	10.18

Note. — Columns are : (1) Galaxy name; (2) Hubble type from RC3 (de Vaucouleurs et al. 1991); (3) RC3 bar type, which is based on visual inspection of optical images and runs as ‘B’=‘strongly barred’, ‘AB’=‘weakly barred’, and ‘A’=‘unbarred’; (4) Distance in Mpc. Most values are from the NBG (Tully 1988), which assumes a Hubble constant of $75 \text{ km s}^{-1} \text{ Mpc}^{-1}$. Exceptions are NGC 6753, NGC 6782, NGC 5078, NGC 6907, NGC 7814, and ESO 142-19, for which distances from RC3 are used; (5) D_{25} in arcminutes, the diameter of the isophote where the B band surface brightness is 25 magnitude arcsecond $^{-2}$. Values are from the NBG, except for NGC 6753, NGC 6782, NGC 5078, NGC 6907, NGC 7814, and ESO 142-19 where RC3 data are used; (6) B_T , the total blue magnitude from RC3; (7) M_V , the absolute V magnitude from RC3; (8) L_{IR} , the global IR luminosity ($8 - 1000 \mu\text{m}$) in units of $\log(L_\odot)$, from the IRAS Revised Bright Galaxy Sample (Sanders et al. 2003); (9) L_B , the global blue luminosity in units of $\log(L_\odot)$, from the RC3.

TABLE 2
BAR STATISTICS FROM SAMPLE S4 (136 GALAXIES)

Band	Unbarred	Barred
B (observed)	75 = 55%	61 = 45%
H (observed)	57 = 42%	79 = 58%
B (deprojected)	76 = 56%	60 = 44%
H (deprojected)	54 = 40%	82 = 60%

Note. — Columns are : (1) Band (observed or deprojected); (2) Number and fraction of galaxies classified as unbarred; (3) Number and fraction of galaxies classified as barred.

TABLE 3
STRUCTURAL PROPERTIES OF SAMPLE S4 (136 GALAXIES) IN B AND H

Galaxy Name	i ($^{\circ}$)	PA_{disk}	class (B)	e_{bar} (B)	a_{bar} (B) (kpc)	class (H)	e_{bar} (H)	a_{bar} (H) (kpc)
(1)	(2)	(3)	(4)	(5)	(6)	(7)	(8)	(9)
IC 0239	37	171	u	-	-	-	-	-
IC 4444	36	77	u	-	-	u	-	-
IC 5325	38	34	u	-	-	b	0.5	1.5
NGC 0157	41	43	u	-	-	u	-	-
NGC 0210	49	160	b	0.6	12.3	b	0.4	9.7
NGC 0278	25	161	u	-	-	u	-	-
NGC 0289	35	162	u	-	-	b	0.6	2.1
NGC 0428	47	109	u	-	-	u	-	-
NGC 0488	38	6	u	-	-	u	-	-
NGC 0685	35	95	b	0.6	2.0	b	0.6	1.2
NGC 0864	43	31	b	0.7	4.2	b	0.6	3.5
NGC 1042	40	173	b	0.6	4.6	b	0.6	4.4
NGC 1058	13	79	u	-	-	u	-	-
NGC 1073	24	174	b	0.7	4.2	b	0.7	4.5
NGC 1084	39	58	u	-	-	b	0.4	6.1
NGC 1087	52	4	u	-	-	u	-	-
NGC 1187	30	130	b	0.7	3.5	b	0.5	2.9
NGC 1241	55	151	b	0.6	3.8	b	0.6	4.1
NGC 1300	55	102	b	0.6	8.4	b	0.5	8.5
NGC 1302	22	13	b	0.3	2.9	b	0.3	2.9
NGC 1309	21	64	u	-	-	u	-	-
NGC 1317	29	171	b	0.4	0.6	b	0.4	0.6
NGC 1350	58	2	u	-	-	b	0.5	6.8
NGC 1371	24	81	u	-	-	b	0.4	1.9
NGC 1385	47	24	b	0.8	2.0	b	0.6	1.7
NGC 1493	21	90	u	-	-	b	0.5	1.2
NGC 1559	56	61	b	0.8	1.7	b	0.5	0.9
NGC 1617	58	109	u	-	-	u	-	-
NGC 1637	35	31	b	0.5	1.2	b	0.4	1.0
NGC 1703	30	134	u	-	-	b	0.3	1.3
NGC 1792	50	139	u	-	-	b	0.5	4.2
NGC 1832	48	11	b	0.6	2.5	b	0.4	2.2
NGC 2139	36	154	u	-	-	u	-	-
NGC 2196	45	57	u	-	-	u	-	-
NGC 2566	24	59	b	0.6	4.9	b	0.5	4.7
NGC 2775	24	24	u	-	-	u	-	-
NGC 2964	49	95	b	0.6	2.6	b	0.5	2.6
NGC 3166	56	77	u	-	-	b	0.5	3.8
NGC 3169	55	58	u	-	-	u	-	-
NGC 3223	47	117	u	-	-	u	-	-
NGC 3227	55	151	u	-	-	u	-	-
NGC 3261	28	59	b	0.5	5.4	b	0.4	3.7
NGC 3275	21	150	b	0.6	7.6	b	0.5	6.6
NGC 3423	39	35	u	-	-	u	-	-
NGC 3504	8	79	b	0.6	3.8	b	0.6	4.1
NGC 3507	21	67	b	0.5	2.9	b	0.5	2.6
NGC 3513	43	63	b	0.8	2.7	b	0.7	2.1
NGC 3583	39	134	u	-	-	b	0.5	4.4
NGC 3593	57	86	u	-	-	u	-	-
NGC 3596	32	81	u	-	-	u	-	-
NGC 3646	56	56	u	-	-	u	-	-
NGC 3681	24	132	b	0.3	1.1	b	0.3	0.9
NGC 3684	47	127	u	-	-	u	-	-
NGC 3686	33	18	b	0.7	2.7	b	0.5	2.6
NGC 3726	52	13	b	0.7	4.0	b	0.6	3.8
NGC 3810	45	17	u	-	-	u	-	-
NGC 3885	58	114	u	-	-	u	-	-
NGC 3887	44	13	b	0.6	3.7	b	0.5	3.3
NGC 3893	48	10	u	-	-	b	0.5	6.0
NGC 3938	30	13	u	-	-	u	-	-
NGC 3949	16	143	u	-	-	u	-	-
NGC 4027	38	176	u	-	-	b	0.6	1.2
NGC 4030	43	21	u	-	-	u	-	-
NGC 4051	30	116	b	0.6	4.2	b	0.6	4.8
NGC 4123	43	121	b	0.6	10.5	b	0.6	4.2
NGC 4136	20	51	b	0.6	1.7	b	0.4	0.7
NGC 4145	57	98	b	0.6	1.4	b	0.5	1.7
NGC 4151	36	2	u	-	-	b	0.5	7.9
NGC 4212	43	72	u	-	-	b	0.4	2.8
NGC 4242	45	22	u	-	-	b	0.3	3.0
NGC 4254	24	59	u	-	-	u	-	-
NGC 4303	30	144	b	0.7	3.3	b	0.5	4.5
NGC 4314	18	38	b	0.6	3.2	b	0.6	3.7
NGC 4394	24	109	b	0.5	4.0	b	0.5	3.6
NGC 4414	44	166	u	-	-	u	-	-
NGC 4450	44	174	b	0.4	3.8	b	0.4	3.6
NGC 4457	25	86	u	-	-	u	-	-
NGC 4487	48	72	u	-	-	b	0.3	1.0

TABLE 3—*Continued*

Galaxy Name	i ($^{\circ}$)	PA_{disk}	class (B)	e_{bar} (B)	a_{bar} (B) (kpc)	class (H)	e_{bar} (H)	a_{bar} (H) (kpc)
(1)	(2)	(3)	(4)	(5)	(6)	(7)	(8)	(9)
NGC 4496	24	65	b	0.7	2.1	b	0.6	0.8
NGC 4504	55	147	u	-	-	u	-	-
NGC 4548	40	154	b	0.6	6.2	b	0.6	5.9
NGC 4571	33	36	u	-	-	u	-	-
NGC 4579	35	95	b	0.4	3.9	b	0.4	3.7
NGC 4580	43	161	b	0.6	4.3	b	0.3	1.9
NGC 4593	43	105	b	0.6	13.6	b	0.6	12.9
NGC 4618	25	178	u	-	-	b	0.6	0.5
NGC 4643	34	56	b	0.5	7.1	b	0.5	5.4
NGC 4647	50	121	b	0.6	2.5	u	-	-
NGC 4651	49	71	u	-	-	u	-	-
NGC 4665	33	17	b	0.3	3.8	b	0.4	4.1
NGC 4689	44	173	u	-	-	u	-	-
NGC 4691	34	27	u	-	-	b	0.7	2.01
NGC 4698	59	174	u	-	-	b	0.5	2.6
NGC 4699	33	34	b	0.3	1.7	b	0.3	1.5
NGC 4775	18	47	u	-	-	u	-	-
NGC 4900	22	113	b	0.8	5.4	b	0.6	1.8
NGC 4902	16	102	b	0.6	6.8	b	0.5	4.7
NGC 4930	40	52	b	0.5	8.1	b	0.4	8.0
NGC 4939	53	6	u	-	-	u	-	-
NGC 4941	58	13	u	-	-	u	-	-
NGC 4995	47	93	b	0.6	6.3	b	0.5	3.7
NGC 5005	59	59	u	-	-	u	-	-
NGC 5054	52	159	u	-	-	u	-	-
NGC 5085	32	56	u	-	-	u	-	-
NGC 5101	23	65	b	0.5	7.3	b	0.5	6.8
NGC 5121	48	57	u	-	-	u	-	-
NGC 5247	36	36	u	-	-	u	-	-
NGC 5334	41	11	b	0.6	3.0	b	0.5	1.8
NGC 5371	40	31	b	0.5	6.5	b	0.4	19.7
NGC 5427	38	11	u	-	-	b	0.5	4.8
NGC 5483	34	50	u	-	-	u	-	-
NGC 5676	59	50	u	-	-	u	-	-
NGC 5701	24	43	b	0.4	5.8	b	0.4	5.3
NGC 5713	32	1	u	-	-	b	0.6	3.5
NGC 5850	29	178	b	0.7	12.1	b	0.6	10.6
NGC 5921	46	130	b	0.7	8.5	b	0.6	7.6
NGC 5962	42	109	u	-	-	u	-	-
NGC 6215	44	43	u	-	-	b	0.5	1.8
NGC 6300	38	109	b	0.7	3.0	b	0.5	2.8
NGC 6384	55	27	u	-	-	u	-	-
NGC 6753	30	25	u	-	-	u	-	-
NGC 6782	28	36	b	0.5	6.7	b	0.4	6.4
NGC 6902	22	162	u	-	-	b	0.3	3.3
NGC 6907	51	65	u	-	-	u	-	-
NGC 7083	54	8	u	-	-	u	-	-
NGC 7205	58	65	u	-	-	u	-	-
NGC 7213	18	179	u	-	-	u	-	-
NGC 7217	30	136	u	-	-	u	-	-
NGC 7412	52	74	b	0.6	1.8	b	0.6	6.6
NGC 7418	27	91	b	0.7	2.6	b	0.6	2.8
NGC 7479	41	33	b	0.7	8.0	b	0.6	8.6
NGC 7552	23	33	b	0.7	2.0	b	0.6	5.3
NGC 7713	59	166	u	-	-	u	-	-
NGC 7723	34	38	b	0.6	3.2	b	0.5	2.3
NGC 7727	16	64	u	-	-	u	-	-
NGC 7741	40	167	b	0.7	3.2	b	0.6	3.0

Note. — Columns are : (1) Galaxy name; (2) Outer disk inclination i , calculated from B band ellipse fits before deprojection; (3) Outer disk PA, calculated from B band ellipse fits before deprojection; (4) B band classification as unbarred (u) or barred (b) from ellipse fits after deprojection; (5) Bar strength, as characterized by e_{bar} , of large-scale bar in B band after deprojection; (6) Bar semi-major axis a_{bar} in kpc of large-scale bar in B band after deprojection; (7) H band classification as unbarred (u) or barred (b) from ellipse fits after deprojection; (8) Bar strength, as characterized by e_{bar} , of large-scale bar in H band after deprojection; (9) Bar semi-major axis a_{bar} in kpc of large-scale bar in H band after deprojection.